



## Scale and Rossby Number Dependence of Observed Wind Responses to Ocean-Mesoscale Sea Surface Temperatures

NIKLAS SCHNEIDER

*International Pacific Research Center, and Department of Oceanography, University of Hawai'i at Mānoa, Honolulu, Hawaii*

(Manuscript received 23 May 2020, in final form 4 June 2020)

### ABSTRACT

The horizontal scale dependences of in-phase and lagged imprints of ocean-mesoscale sea surface temperatures on surface winds are investigated using daily AMSR-E radiometer and QuikSCAT scatterometer observations in the Southern Ocean. Spectral transfer functions separate underlying processes dependent on large-scale winds, horizontal wavenumbers, and corresponding Rossby numbers. For Rossby numbers smaller than 1, winds reflect modulations of the Ekman layer by sea surface temperature–induced changes of hydrostatic pressure. Rossby numbers large compared to 1 suggest a balance of advection and modulations of vertical mixing. Impulse response functions reveal Southern Hemisphere, Doppler-shifted, near-inertial lee waves excited by warm ocean-mesoscale sea surface temperatures. On the right (left) flank of the downwind wake of warm air and low atmospheric pressure, winds are enhanced (diminished) due to constructive (destructive) interference of inertial turning, pressure gradient forces, and vertical mixing. Wind convergence over the warm wake is stronger compared to the upwind divergence. Time averaging smooths the response, and degrades the lee wave.


### 1. Introduction

Satellite observations have revealed an ubiquitous imprint of ocean-mesoscale sea surface temperature on surface equivalent neutral wind and wind stress (Chelton et al. 2004; Chelton and Xie 2010; Small et al. 2008). Here, we estimate from satellite observations spectral transfer and corresponding impulse response functions and show that underlying dynamics depend on horizontal scale and Rossby number.

The relationship between anomalous sea surface temperature and surface winds has long been recognized to depend on horizontal scale (Small et al. 2008). For scales of the atmospheric baroclinic Rossby radius of deformation and larger, about 1000 km in midlatitudes, winds affect the surface heat budget through changes of the air–sea heat fluxes, such that higher wind speeds cool the surface ocean, and anomalies of wind speed and sea surface temperature are correlated negatively

(Xie 2004; Laurindo et al. 2019). In contrast, for scales associated with ocean-mesoscale eddies and fronts, higher wind speeds occur over warmer ocean waters, and wind speed and sea surface temperatures are correlated positively. The latter relationship is typically characterized by “coupling” coefficients independent of scale, namely, the regressions of frontal-scale wind stress or equivalent neutral winds and sea surface temperature. Coupling coefficients between wind or wind stress magnitudes and sea surface temperature, wind or wind stress divergences and downwind sea surface temperature gradients, and wind or wind stress curls and cross-wind sea surface temperature gradients (Song et al. 2009, and others) vary regionally (Chelton et al. 2004; O’Neill et al. 2005) and seasonally (O’Neill et al. 2005; Maloney and Chelton 2006), and, for numerical models, depend on model resolution and formulation (Bryan et al. 2010; O’Neill et al. 2010b; Seo et al. 2007; Song et al. 2009).

Within the ocean mesoscale, observations and models suggest scale dependence of the wind–sea surface temperature relationships. Heat and momentum budgets of the atmospheric boundary layer depend on length scales of sea surface temperature, on background winds, and

 Denotes content that is immediately available upon publication as open access.

*Corresponding author:* Niklas Schneider, nschneid@hawaii.edu

DOI: 10.1175/JAS-D-20-0154.1

© 2020 American Meteorological Society. For information regarding reuse of this content and general copyright information, consult the [AMS Copyright Policy](#) ([www.ametsoc.org/PUBSReuseLicenses](http://www.ametsoc.org/PUBSReuseLicenses)).

include, through advection and pressure gradients, both in-phase and lagged components (Small et al. 2003, 2005; Spall 2007; Small et al. 2008; O'Neill et al. 2010b). Surface wind divergence is sensitive to the speed and direction of large-scale winds relative to sea surface temperatures of fronts and eddies (Foussard et al. 2019). Observed responses of wind direction are meridionally displaced relative to sea surface temperature and associated phase shifts depend on meridional scales (O'Neill et al. 2010a).

The linear theory of Schneider and Qiu (2015) illustrates this scale dependence, and suggests that the Rossby number delineates the roles of advection and of sea surface temperature–induced vertical mixing and hydrostatic pressure gradients. The theory considers an atmospheric boundary layer bounded by a material inversion, with a large-scale, horizontal background wind with unit vector  $\hat{\mathbf{e}}_U$  and speed  $U$  blowing across an ocean-mesoscale sea surface temperature field  $T$ . For amplitudes sufficiently small to permit linearization of dynamics about the large-scale winds, the steady-state heat budget for vertically homogeneous potential air temperature  $\Theta$

$$\overline{U\hat{\mathbf{e}}_U} \cdot \nabla\Theta = \gamma(T - \Theta) \quad (1)$$

balances horizontal advection by vertically averaged background winds, denoted by an overbar, with the air–sea fluxes proportional to air–sea temperature differences with rate  $\gamma$ . Following Schneider and Qiu (2015), the resulting  $\Theta$  introduces forces  $\mathbf{F}$  in the horizontal momentum equations,

$$\mathbf{F} = \frac{gH}{\Theta_0}(1-s)\nabla\Theta + (T - \Theta)\frac{1}{H^2}\partial_s[A'_m\partial_s(U\hat{\mathbf{e}}_U)], \quad (2)$$

due to the hydrostatic pressure gradient (Lindzen and Nigam 1987) and changes of vertical mixing (Wallace et al. 1989; Hayes et al. 1989), as first and second terms on the right-hand side of Eq. (2), respectively, with  $g$  Earth's gravitational acceleration,  $H$  the background inversion height,  $\Theta_0$  a reference atmospheric temperatures, and  $s$  the sigma vertical coordinate that varies between 0 at the sea surface and 1 at the inversion. Vertical eddy coefficients  $A_m$  depend on the stability and air–sea buoyancy fluxes, as represented by the sensitivity  $A'_m$  to air–sea temperature differences.

For a spatially variable sea surface temperature field with wavenumber  $\mathbf{k}$ , the ratio  $\mathbf{k} \cdot \hat{\mathbf{e}}_U U/\gamma$  determines regimes in Eq. (1) for air temperature and air–sea fluxes, and in Eq. (2) for hydrostatic pressure and vertical mixing (Small et al. 2008). For  $\mathbf{k} \cdot \hat{\mathbf{e}}_U U/\gamma \gg 1$ , advective terms dominate, air temperature and hydrostatic

pressure changes are small, and air–sea temperature differences, fluxes and vertical mixing effect are large. For  $\mathbf{k} \cdot \hat{\mathbf{e}}_U U/\gamma \ll 1$ , sea surface temperatures imprint on air temperatures and hydrostatic pressure, while air–sea heat fluxes and the vertical mixing effect are small.

Thermal adjustment times of the boundary layer  $\gamma^{-1}$  are on the order of a few hours to half a day (Schubert et al. 1979), so that the ratio  $\gamma/|f|$  is of order 0.2–1 for a Coriolis frequency with magnitude  $|f| = 10^{-4} \text{ s}^{-1}$  at  $45^\circ$  latitude. This implies that regimes dominated by vertical mixing and hydrostatic pressure are separated by a Rossby number  $\mathbf{k} \cdot \hat{\mathbf{e}}_U U/|f| = O(0.2-1)$ , so that the Rossby number both compares momentum advection to the Coriolis force and scales the ocean-mesoscale sea surface temperature–induced vertical mixing and hydrostatic pressure.

For Rossby numbers much smaller than 1, that is, for weak background winds  $U$  or wavenumbers  $\mathbf{k}$  in the crosswind direction, advection is unimportant, and dynamics are that of a bottom Ekman layer in the presence of sea surface temperature–induced baroclinic pressure gradients (Feliks et al. 2004), with wind curl and divergence proportional to the Laplacian of sea surface temperature (Feliks et al. 2004; Minobe et al. 2008; Lambaerts et al. 2013; Foussard et al. 2019). Interactions of the wind stress curl with the free troposphere (Feliks et al. 2004) reduce, in the simplest case of a passive free troposphere, to adjustments of atmospheric pressure in the lower troposphere associated with geostrophic spindown (Schneider and Qiu 2015; Kilpatrick et al. 2016). For Rossby numbers much larger than 1, advection and modulations of vertical mixing dominate and are expected to yield wind divergences proportional to downwind gradients of sea surface temperature (Chelton et al. 2001; O'Neill et al. 2003; Foussard et al. 2019). For sufficiently swift background winds, atmospheric boundary layer wind divergences excite vertically propagating gravity waves in the troposphere (Kilpatrick et al. 2014).

Schneider and Qiu (2015) hypothesize that the scale-dependent response of the atmospheric boundary layer to sea surface temperature is described by complex, spectral transfer functions that depend on large-scale background wind speed, and on wavenumbers relative to the background wind direction. Transfer and corresponding impulse response functions are the fundamental patterns in spectral and physical space, respectively, that determine wind responses to any ocean-mesoscale sea surface temperature field. It is the aim of this contribution to elucidate underlying physics by the estimation of such transfer and impulse response functions from satellite observed equivalent neutral winds and ocean-mesoscale sea surface temperature. Sections 2, 3, and 4

introduce transfer functions, their estimation from satellite observations and the skill of the reconstruction. The transfer functions for equivalent neutral winds, wind divergence and curl reveal distinct physics as a function of the Rossby number (section 5). Impulse response functions are presented in section 6. Since the dynamics critically depend on large-scale winds that vary with atmospheric weather, we discuss the impact of averaging (section 7) before concluding (section 8). Appendixes outline application of results to linearized winds stress, and review the theory of Schneider and Qiu (2015).

**2. Transfer function hypothesis**

Horizontal winds  $\mathbf{u}_T$  are composed of background winds  $U\hat{\mathbf{e}}_U$  at spatial scales of order 1000 km and larger, and components  $\mathbf{u}$  at spatial scales commensurate with the ocean mesoscale

$$\mathbf{u}_T = U\hat{\mathbf{e}}_U + \mathbf{u} \tag{3}$$

that are associated with atmospheric fronts, orography, and ocean-mesoscale sea surface temperature. The latter is of interest here, and has root-mean-square speed variations of order  $0.5 \text{ m s}^{-1}$ , much less than typical  $U$  values of  $10 \text{ m s}^{-1}$ . This justify linearizations about background winds of wind speed and direction used below.

*a. Lee and port coordinates*

Background winds are the only deviation from an otherwise horizontally isotropic  $f$  plane, and determine the natural coordinate system spanned by the upward unit vector  $\hat{\mathbf{e}}_3$ , by  $\hat{\mathbf{e}}_U$ , and by the horizontal unit vector to the left of the background wind  $\hat{\mathbf{e}}_3 \times \hat{\mathbf{e}}_U$ . Ocean-mesoscale horizontal wind components  $u_1$  in direction of background winds

$$u_1 = \hat{\mathbf{e}}_U \cdot \mathbf{u} \tag{4}$$

and  $u_2$  across the background winds

$$u_2 = (\hat{\mathbf{e}}_3 \times \hat{\mathbf{e}}_U) \cdot \mathbf{u} \tag{5}$$

measure changes of  $\mathbf{u}_T$  speed and direction, respectively, linearized about background winds (Schneider and Qiu 2015). Wind divergence

$$\nabla \cdot \mathbf{u} = (\hat{\mathbf{e}}_U \cdot \nabla)u_1 + [(\hat{\mathbf{e}}_3 \times \hat{\mathbf{e}}_U) \cdot \nabla]u_2 \tag{6}$$

is caused by downwind changes of the wind speed and crosswind gradient of wind direction, where down- and crosswind are relative to background winds, and

$\nabla$  is the nabla operator. The vertical component of the wind curl

$$\hat{\mathbf{e}}_3 \cdot (\nabla \times \mathbf{u}) = (\hat{\mathbf{e}}_U \cdot \nabla)u_2 - [(\hat{\mathbf{e}}_3 \times \hat{\mathbf{e}}_U) \cdot \nabla]u_1 \tag{7}$$

results from downwind turning of the winds, and crosswind changes of the wind speed (O’Neill et al. 2010a).

In the following, directions  $\hat{\mathbf{e}}_U$  and  $\hat{\mathbf{e}}_3 \times \hat{\mathbf{e}}_U$  are called “lee” and “port,” respectively, using nautical terms for downwind and left. Components  $u_1$  and  $u_2$  are the lee and port components of ocean-mesoscale winds,  $\hat{\mathbf{e}}_U \cdot \nabla$  and  $(\hat{\mathbf{e}}_3 \times \hat{\mathbf{e}}_U) \cdot \nabla$  are the lee and port components of the gradient, and  $\hat{\mathbf{e}}_U \cdot \mathbf{k}$  and  $(\hat{\mathbf{e}}_3 \times \hat{\mathbf{e}}_U) \cdot \mathbf{k}$  denote lee and port components of the horizontal wavenumber.

*b. Transfer function ansatz*

To investigate the horizontal scale dependence of the wind response to mesoscale sea surface temperature  $T$ , variables are Fourier transformed to wavenumber space

$$u_j(\mathbf{x}) = (2\pi)^{-2} \int d\mathbf{k} \tilde{u}_j(\mathbf{k}) e^{-i\mathbf{k}\cdot\mathbf{x}}, \quad j = 1, 2, \tag{8}$$

$$T(\mathbf{x}) = (2\pi)^{-2} \int d\mathbf{k} \tilde{T}(\mathbf{k}) e^{-i\mathbf{k}\cdot\mathbf{x}}, \tag{9}$$

where the tilde denotes Fourier amplitudes,  $\mathbf{x}$  the location vector in local Cartesian coordinates,  $i = \sqrt{-1}$ , and  $d\mathbf{k}$  indicates integrations over both horizontal wavenumber components.

Schneider and Qiu (2015) hypothesized that Fourier amplitudes of lee and port wind responses are linearly dependent on those of sea surface temperature at the same wavenumber  $\mathbf{k}$

$$\tilde{u}_j(\mathbf{k}) = \tilde{A}_j [\hat{\mathbf{e}}_U \cdot \mathbf{k}, (\hat{\mathbf{e}}_3 \times \hat{\mathbf{e}}_U) \cdot \mathbf{k}, U] \tilde{T}(\mathbf{k}) + \xi \tilde{u}_j(\mathbf{k}), \tag{10}$$

$j = 1, 2.$

Residuals  $\xi u_j(\mathbf{x})$ , and their Fourier amplitudes  $\xi \tilde{u}_j(\mathbf{k})$ ,  $j = 1, 2$ , encompass wind variations independent of mesoscale sea surface temperatures.

Regression coefficients  $\tilde{A}_1$  and  $\tilde{A}_2$  in Eq. (10) are the complex transfer functions of lee and port winds, respectively. Their magnitudes are the gain, and their phases describe the lag between  $\tilde{T}(\mathbf{k})$  and the wind components. Positive real parts of  $\tilde{A}_j$  capture maxima of lee and port winds that are in phase with warmest sea surface temperatures. Positive imaginary parts of  $\tilde{A}_j$  describe lee and port winds lagged by a quarter period, so that maxima of winds are  $180^\circ$  out of phase with sea surface temperature gradients.

The reality condition implies that

$$\tilde{A}_j(-\mathbf{k}, U) = \tilde{A}_j^*(\mathbf{k}, U), \quad j = 1, 2, \tag{11}$$

where the superscript asterisk (\*) indicates the complex conjugate.

Theory predicts that  $\tilde{A}_j$  are functions of the lee and port components of the wavenumbers,  $\hat{\mathbf{e}}_U \cdot \mathbf{k}$  and  $(\hat{\mathbf{e}}_3 \times \hat{\mathbf{e}}_U) \cdot \mathbf{k}$ , and of the background wind speed  $U$  (Schneider and Qiu 2015). This dependence on background wind direction within the ocean mesoscale is in contrast to transfer functions in geographically fixed, zonal wavenumbers that are used to distinguish the relationship between sea surface temperature and wind speed at large scales and at the ocean mesoscale (Small et al. 2008; O'Neill 2012; Laurindo et al. 2019).

With ansatz (10) and (8), the lee and port components of the wind in physical space are determined by the Fourier coefficients of sea surface temperature as

$$u_j(\mathbf{x}) = (2\pi)^{-2} \int d\mathbf{k} \tilde{A}_j[\hat{\mathbf{e}}_U \cdot \mathbf{k}, (\hat{\mathbf{e}}_3 \times \hat{\mathbf{e}}_U) \cdot \mathbf{k}, U] \tilde{T}(\mathbf{k}) e^{-i\mathbf{k} \cdot \mathbf{x}} + \xi u_j(\mathbf{x}), \quad j = 1, 2. \quad (12)$$

Applications of (12) to (6) and (7) show the relations between transfer functions  $\tilde{A}_3$  and  $\tilde{A}_4$  for wind divergence and curl and  $\tilde{A}_1$  and  $\tilde{A}_2$  for lee and port wind components

$$\nabla \cdot \mathbf{u} = (2\pi)^{-2} \int d\mathbf{k} (-i) \underbrace{[\hat{\mathbf{e}}_U \cdot \mathbf{k} \tilde{A}_1 + (\hat{\mathbf{e}}_3 \times \hat{\mathbf{e}}_U) \cdot \mathbf{k} \tilde{A}_2]}_{\tilde{A}_3[\hat{\mathbf{e}}_U \cdot \mathbf{k}, (\hat{\mathbf{e}}_3 \times \hat{\mathbf{e}}_U) \cdot \mathbf{k}, U]} \times \tilde{T}(\mathbf{k}) e^{-i\mathbf{k} \cdot \mathbf{x}} + \nabla \cdot \xi \mathbf{u}, \quad (13)$$

$$\hat{\mathbf{e}}_3 \cdot (\nabla \times \mathbf{u}) = (2\pi)^{-2} \int d\mathbf{k} (-i) \underbrace{[\hat{\mathbf{e}}_U \cdot \mathbf{k} \tilde{A}_2 - (\hat{\mathbf{e}}_3 \times \hat{\mathbf{e}}_U) \cdot \mathbf{k} \tilde{A}_1]}_{\tilde{A}_4[\hat{\mathbf{e}}_U \cdot \mathbf{k}, (\hat{\mathbf{e}}_3 \times \hat{\mathbf{e}}_U) \cdot \mathbf{k}, U]} \times \tilde{T}(\mathbf{k}) e^{-i\mathbf{k} \cdot \mathbf{x}} + \hat{\mathbf{e}}_3 \cdot (\nabla \times \xi \mathbf{u}), \quad (14)$$

In Eqs. (13) and (14), terms proportional to the real parts of  $\tilde{A}_1$  are the spectral counterparts to coupling coefficients between divergence and lee, and between curl and port components of sea surface temperature gradients (Chelton et al. 2001, 2004), since  $-i[\hat{\mathbf{e}}_U \cdot \mathbf{k}, (\hat{\mathbf{e}}_3 \times \hat{\mathbf{e}}_U) \cdot \mathbf{k}] \tilde{T}(\mathbf{k})$  is the surface temperature gradient in wavenumber space. Positive real parts of  $\tilde{A}_1$  correspond to observed relationships between positive wind divergence (curl) and positive lee (negative port) components of the sea surface temperature gradients (O'Neill et al. 2005). Differences in transfer functions for divergence and curl result from terms proportional to  $\tilde{A}_2$ , and from the fact that  $\tilde{A}_1$  and  $\tilde{A}_2$  terms are added for divergence, and are subtracted for the curl (O'Neill et al. 2010a).

### c. Impulse response functions

Equations (12)–(14) are identical to convolutions of sea surface temperature and impulse response functions

$$u_j(\mathbf{x}) = \int d\mathbf{x}' A_j[\hat{\mathbf{e}}_U \cdot (\mathbf{x} - \mathbf{x}'), (\hat{\mathbf{e}}_3 \times \hat{\mathbf{e}}_U) \cdot (\mathbf{x} - \mathbf{x}'), U] T(\mathbf{x}') + \xi u_j(\mathbf{x}), \quad j = 1, \dots, 4, \quad (15)$$

where  $j = 3$  and  $j = 4$  correspond to the wind divergence and curl, respectively. The impulse response functions  $A_j$  are the inverse Fourier transform of the transfer functions  $\tilde{A}_j$

$$A_j[\hat{\mathbf{e}}_U \cdot \mathbf{x}, (\hat{\mathbf{e}}_3 \times \hat{\mathbf{e}}_U) \cdot \mathbf{x}, U] = (2\pi)^{-2} \int d\mathbf{k} \tilde{A}_j[\hat{\mathbf{e}}_U \cdot \mathbf{k}, (\hat{\mathbf{e}}_3 \times \hat{\mathbf{e}}_U) \cdot \mathbf{k}, U] e^{-i\mathbf{k} \cdot \mathbf{x}}, \quad j = 1, \dots, 4. \quad (16)$$

Equation (15) determines winds at a particular position from sea surface temperature everywhere, with weights given by the impulse response functions  $A_j$ . These depend on lee and port components of the spatial lag  $\mathbf{x} - \mathbf{x}'$  between winds and surface temperature and on background wind speeds.

### d. Relationship to coupling coefficients

Transfer functions consider lags and scale dependence and generalize coupling coefficients that relate collocated winds and sea surface temperatures. Coupling coefficients  $\alpha_j$  corresponds to the special case of transfer functions that are constant for all wavenumbers,  $\tilde{A}_j = \alpha_j(U)$  and impulse response functions that are nontrivial for zero lag only,  $A_j = \alpha_j(U) \delta(\mathbf{x} - \mathbf{x}')$ , where  $\delta$  is the Dirac delta function. For this case, Eqs. (12) and (15) reduce to a local regression between winds and sea surface temperatures and recover the coupling coefficient ansatz.

## 3. Estimation of transfer functions

We estimate transfer functions  $\tilde{A}_j$ ,  $j = 1, 2$  at discrete values of lee and port wavenumbers  $\mathbf{k}_0$  and speeds  $U_0$  by fitting satellite observations of equivalent neutral winds and sea surface temperature to Eq. (12), and obtain transfer functions for wind divergence and curl from Eqs. (13) and (14), and impulse response functions from Eq. (16).<sup>1</sup>

### a. QuikSCAT equivalent neutral winds and AMSR-E sea surface temperatures

The determination of transfer functions in the presence of large residuals associated with atmospheric weather requires many observed realizations of surface

<sup>1</sup> Alternatively, impulse response functions could be determined by a fit to the data, and the transfer functions from the Fourier transform of the impulse response function.

winds and temperature. Twice daily Quick Scatterometer (QuikSCAT), version 4, equivalent neutral winds at a height of 10 m (Ricciardulli et al. 2011) and running 3-day averages of Advanced Microwave Scanning Radiometer for EOS (AMSR-E) sea surface temperatures, version 7 (Wentz et al. 2014), were prepared and projected onto 0.25° latitude–longitude grids by Remote Sensing System. We use these data in the Southern Ocean south of the Agulhas Retroflection, 52°–36°S, 12°–52°E from 2003 to 2008 when QuikSCAT and AMSR-E observations overlap. Scatterometer observations flagged as contaminated by rain are excluded. Winds are averaged over 1 day since transfer functions imply a quasi-steady response of winds to sea surface temperature, and are appropriate for time scales longer than the inertial and geostrophic spindown time scale of the boundary layer (Schneider and Qiu 2015). The analysis is performed on equivalent neutral winds, that is, the hypothetical winds that would cause the satellite observed stress under neutral stability and zero ocean currents. For short, we will refer to these observations as “winds,” even though the underlying scatterometer observations are a measure of the wind stress (Liu and Tang 1996; Liu et al. 2007), that, for the dearth of available in situ stress data, are calibrated in terms of 10-m equivalent neutral winds (O’Neill et al. 2012; Wentz et al. 2017).

*b. Background winds and Fourier amplitudes*

The 40° longitude × 16° latitude study region in the Southern Ocean is split into 27 squares of 8° latitude × 8° longitude with 50% overlap. Daily averages for the 6 years of data then yield  $N = 58911$  realizations with sufficient wind and sea surface temperature coverage. For each realization, background winds  $U\hat{e}_U$  are estimated as spatial averages, and determine lee and port components of the winds via Eqs. (4) and (5). Using a local Cartesian coordinate on the central latitude, two-dimensional best fit planes are removed from sea surface temperature and from winds to determine mesoscale  $T$  and  $\mathbf{u}$  via the scale separation (3). The resulting spatial high pass fields show the expected collocation of high surface temperature and wind speed (Fig. 1) reported in earlier analysis that employed more sophisticated spatial filtering (O’Neill et al. 2005).

For each realization, sea surface temperature Fourier amplitudes  $\tilde{T}$  are obtained using (9) for eastward  $\hat{e}_{\text{east}} \cdot \mathbf{k}$  and northward  $(\hat{e}_3 \times \hat{e}_{\text{east}}) \cdot \mathbf{k}$  wavenumber components

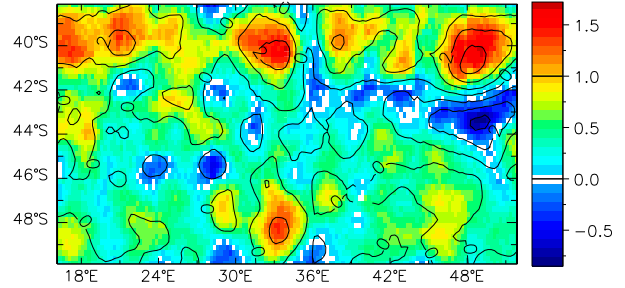


FIG. 1. Wind speed (lee winds) ( $\text{m s}^{-1}$ , color) and sea surface temperature (contours, with an interval of 1 K) in the study region and averaged for the year 2006. Wind speed and sea surface temperature fields have been spatially high-pass filtered as described in section 3.

with resolutions of  $0.156 \times 10^{-5}$  and  $0.112 \times 10^{-5}$  cycles per meter (hereafter,  $\text{cyc m}^{-1}$ ), respectively (Fig. 2). A cutoff at a magnitude of  $1.734 \times 10^{-5} \text{ cyc m}^{-1}$  yields a total of 536 wavenumbers. Least squares fitting is used to allow for missing data and islands, with the inversion of the normal equations regularized by adding a diagonal with a noise variance of  $10^{-2} \text{ K}^2$ . To maximize spectral resolution, a rectangular window is used to estimate Fourier amplitudes. Experiments with different tapering show that spectral leakage does not impact results significantly (R. Masunaga 2020, personal communications).

Fits of winds to the Fourier amplitudes  $\tilde{T}$  via Eq. (12) are performed for the inner 4° latitude × 4° longitude regions to minimize boundary effects and allow for up-wind surface temperature variations. This yields, for the 1/4° spatial resolution and full fields,  $N_x = 256$  spatial points of wind observations.

*c. Transfer functions in lee and port wavenumbers*

Transfer functions at observed lee and port wavenumbers  $\hat{e}_U \cdot \mathbf{k}$ ,  $(\hat{e}_3 \times \hat{e}_U) \cdot \mathbf{k}$  and background wind speeds  $U$  are linked to transfer function values at the target lee and port wavenumbers  $\mathbf{k}_0$  and the target wind speeds  $U_0$  via interpolation

$$\tilde{A}_j[\hat{e}_U \cdot \mathbf{k}, (\hat{e}_3 \times \hat{e}_U) \cdot \mathbf{k}, U] = \sum_{\mathbf{k}_0, U_0} W_{\hat{e}_U, \mathbf{k}, U, \mathbf{k}_0, U_0} \tilde{A}_j(\mathbf{k}_0, U_0), \quad j = 1, 2. \quad (17)$$

Weights  $W$  correspond to linear interpolations of transfer function values within wavenumber and speed search radii  $\lambda$  and  $\Delta$

$$W_{\hat{e}_U, \mathbf{k}, U, \mathbf{k}_0, U_0} = W_0 \max \left\{ 1 - \sqrt{\frac{|\hat{e}_U \cdot \mathbf{k}, (\hat{e}_3 \times \hat{e}_U) \cdot \mathbf{k}| - \mathbf{k}_0|^2}{\lambda^2} + \frac{(U - U_0)^2}{\Delta^2}}, 0 \right\} \quad (18)$$

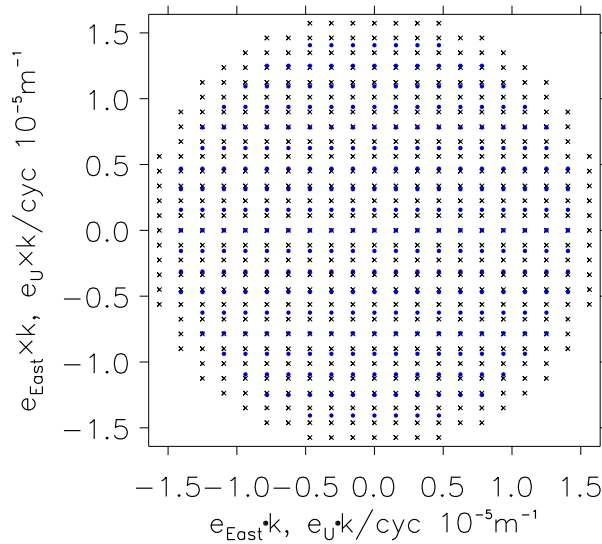


FIG. 2. Wavenumber coverage and resolution for sea surface temperature (crosses) and transfer functions (blue dots). Sea surface temperature wavenumbers are given in eastward and northward components, while target wavenumbers for transfer functions are given in lee and port components relative to the background wind.

with amplitudes  $W_0$  selected such that

$$\sum_{\mathbf{k}_0, U_0} W_{\hat{\mathbf{e}}_U, \mathbf{k}, U, \mathbf{k}_0, U_0} = 1 \quad (19)$$

for every  $\hat{\mathbf{e}}_U$ ,  $\mathbf{k}$ , and  $U$ . Wavenumber and speed search radii  $\lambda$  and  $\Delta$  in Eq. (18) correspond to the target wavenumber and speed resolutions.

Target lee and port wavenumbers  $\mathbf{k}_0$  are chosen to be equal to the eastward component  $\hat{\mathbf{e}}_{\text{east}} \cdot \mathbf{k}$ , but exclude wavenumber magnitudes greater than  $0.9 \max(|\hat{\mathbf{e}}_{\text{east}} \cdot \mathbf{k}|)$ , which yields 316 target wavenumbers with a maximum magnitude of  $1.551 \times 10^{-5} \text{ cyc m}^{-1}$  (Fig. 2). The background wind rose (Fig. 3) captures the expected preponderance of strong westerlies, and suggests 5 target speeds  $U_0$  from 1 to  $21 \text{ m s}^{-1}$  with steps of  $5 \text{ m s}^{-1}$ . This implies that a total of  $N_0 = 1580$  complex transfer function values are estimated for  $\tilde{A}_1$  and for  $\tilde{A}_2$ . With reality condition (11), the number of unknowns are reduced by a factor of 2. Given that the transfer function shown below are smooth, the degrees of freedom of this inversion could be drastically reduced with little penalty in skill. This optimization is left for a future exploration.

#### d. Least squares fitting

With Eqs. (17) and (18), Eq. (12) relates the observed lee and port winds in physical space to transfer functions in the space spanned by target lee and port wavenumbers

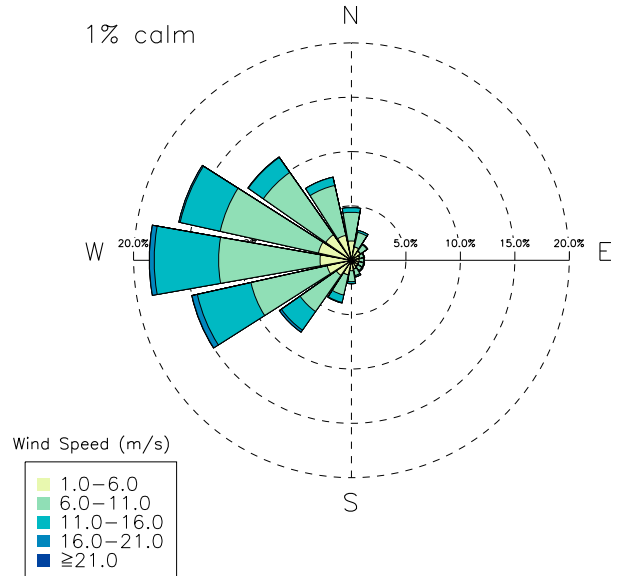


FIG. 3. Wind rose of daily background winds in the Southern Ocean study region for years 2003–08. The radial coordinate denotes the probability (%), the azimuthal direction shows the wind direction. Wind speed is discretized in  $5 \text{ m s}^{-1}$  bins starting at  $1 \text{ m s}^{-1}$ , wind direction is in  $22.5^\circ$  bins.

$\mathbf{k}_0$  and background wind speeds  $U_0$ . Transfer functions  $\tilde{A}_j$ ,  $j = 1, 2$  at lee and port wavenumbers  $\mathbf{k}_0$  and background speeds  $U_0$  are obtained by minimizing the cost function

$$R_j = \frac{1}{N_x N} \sum_{\mathbf{x}, i} [\xi u_j^i(\mathbf{x})]^2 + \frac{r^2}{N_0} \sum_{\mathbf{k}_0, U_0} \tilde{A}_j(\mathbf{k}_0, U_0) \tilde{A}_j^*(\mathbf{k}_0, U_0), \quad j = 1, 2, \quad (20)$$

where  $N_x$  denotes the number of spatial points in the analysis region, the index  $i = 1, N$  indicates the realization, and  $N_0$  is the number of unknown values of  $\tilde{A}_j$  for each  $j = 1, 2$ . The cost function includes, as its first term, the misfit, and, as its second term, a smoothness constraint that regularizes the normal equations. We chose  $r$  to be half of the root-mean square value of the spatially high-pass filtered, daily sea surface temperatures in all  $8^\circ$  latitude  $\times$   $8^\circ$  longitude squares. Increasing  $r$  reduces amplitudes and increases smoothness of the transfer function, but does not qualitatively change their patterns and reconstruction skill.

Variances of the transfer function estimates are obtained from the inverse of the normal matrix, the root-mean-square values of misfits for lee and port wind components, and the degrees of freedom measured as the difference of numbers of observations and unknowns (Wunsch 1996).

TABLE 1. Cross-validated skill scores for the reconstruction of annual averages of lee and port wind components.

	2003	2004	2005	2006	2007	2008
$u_1$	0.84	0.84	0.84	0.85	0.81	0.83
$u_2$	0.70	0.72	0.63	0.77	0.71	0.75

**4. Reconstruction skill**

*a. Cross-validated hindcast*

Cross-validated skills are estimated by reconstructing data from daily sea surface temperature and background winds observations of a particular year by using transfer functions estimated without wind data of that year. Skills of annual averaged reconstruction of lee and port wind components  $S_j, j = 1, 2$  are estimated from residuals as

$$S_j = 1 - \frac{\sum_x \langle \xi u_j \rangle^2}{\sum_x \langle u_j \rangle^2}, \quad j = 1, 2, \quad (21)$$

where  $\langle \dots \rangle$  indicates the time average over the reconstructed year, and sum is taken over space. A skill score of 1 indicates a perfect hindcast, while 0 indicates a skill as good as hindcasts of nil produce.

Cross-validated skills hover around 0.83 and 0.75, respectively, for each analysis year (Table 1). As an example, Fig. 4 shows the 2006 annual averages of observed (Figs. 4a,c) and reconstructed (Figs. 4b,d) lee (Figs. 4a,b) and port (Figs. 4c,d) components of the

winds. The reconstruction of the lee components captures all main features and magnitudes, with a pattern correlation with observations of 0.81 and a skill score of 0.85. Data and reconstruction agree best in the northernmost 4° latitude bin, where sea surface temperature amplitudes are largest (Fig. 1). Comparisons are least favorable in the southeast and southwest regions. Port wind reconstructions recover patterns of the observation well, but with a reduced amplitude, and sport a pattern correlation of 0.88 and a skill score of 0.77.

*b. Sea surface temperature monopole*

Via Eq. (12) or (15), transfer functions enable reconstructions of wind responses to any sea surface temperature distribution and background wind within observed characteristics, including eddies, fronts, and meanders. To compare with observed, propagating eddy composites in the entire Southern Ocean (Frenger et al. 2013) and in its Indian Ocean sector (Gaube et al. 2015), and in preparation for the discussion of impulse response functions, we reconstruct wind responses to a localized sea surface temperature anomaly.

In the Southern Ocean, sea surface temperature signatures of large-amplitude eddies are approximately monopoles (Hausmann and Czaja 2012; Frenger et al. 2013; Gaube et al. 2015), warm for anticyclones, and cool for cyclones. Anticyclonic eddies are associated with a 1-K sea surface temperature perturbation and a  $0.5 \text{ ms}^{-1}$  increase of wind speed, or lee winds in the parlance of this paper. Wind divergences form a dipole aligned with background winds, with positive values on

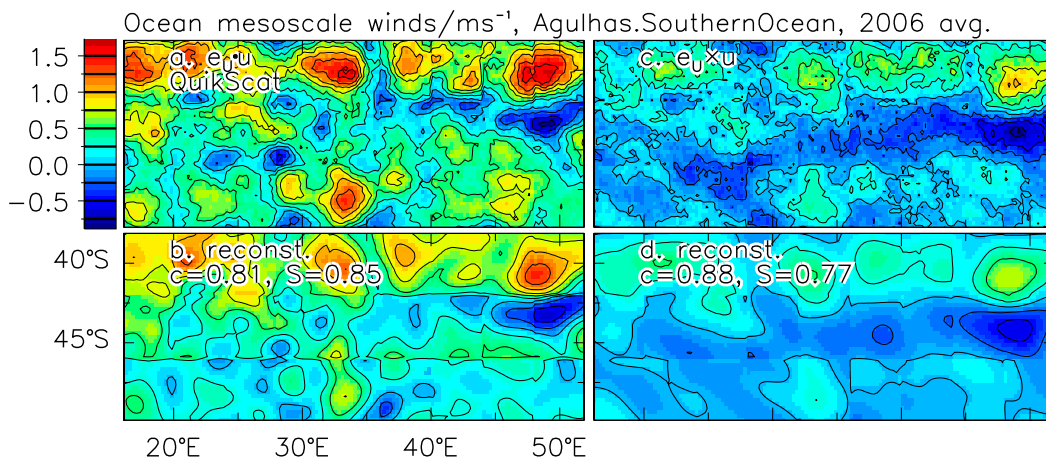


FIG. 4. Daily values of (a),(b) lee and (c),(d) port wind components ( $\text{ms}^{-1}$ ) averaged over the year 2006 for values (a),(c) observed by QuikSCAT, and (b),(d) estimated from cross-validated reconstructions using transfer functions obtained from all years excluding the year 2006. The correlation  $c$  and skill scores  $S$  between observations and cross-validated hindcasts are stated in (b) and (d). Observations are spatially high-pass filtered by removal of the a best-fit linear plane for overlapping  $8^\circ$  latitude  $\times$   $8^\circ$  longitude boxes, and reconstructions are shown for  $4^\circ$  latitude  $\times$   $4^\circ$  longitude inner boxes. Their borders appear as discontinuities in the reconstructions.

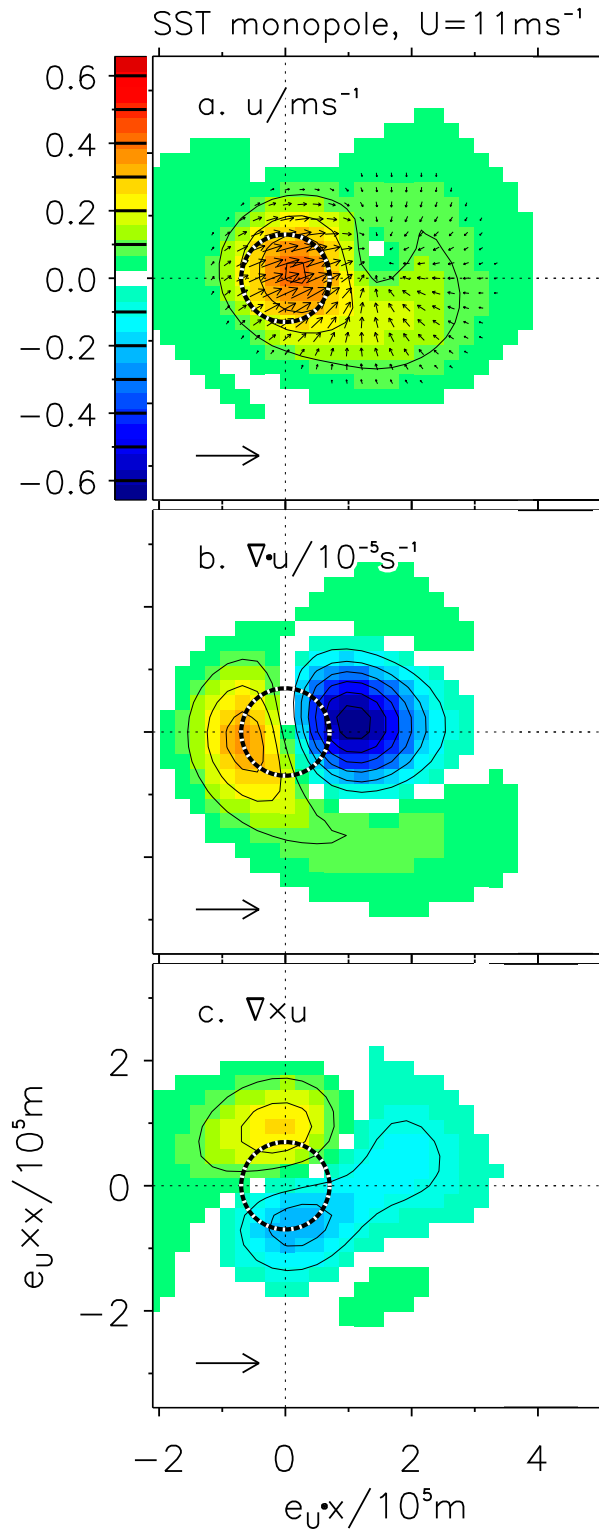


FIG. 5. Response of (a) surface winds ( $\text{m s}^{-1}$ ) and of surface wind (b) divergence and (c) curl ( $10^{-5} \text{ s}^{-1}$ ) to a Gaussian sea surface temperature monopole with amplitude of 1 K, and a background wind blowing from left to right at  $11 \text{ m s}^{-1}$ . Axes are distances in the direction and to the left of background winds (lee and port

the upwind, and negative values on the downwind flanks of the eddy, and magnitudes of  $0.5 \times 10^{-5} \text{ s}^{-1}$  (Frenger et al. 2013). Ekman pumping associated with sea surface temperature perturbations of propagating eddies are estimated for the Agulhas Return Current from coupling coefficient of  $0.025 \text{ N m}^{-2} \text{ K}^{-1}$  between wind stress curl and port sea surface temperature gradient (Gaube et al. 2015). For anticyclonic, warm eddies, Ekman pumping forms a dipole, oriented perpendicular to large-scale winds, and reaches values of  $10 \text{ cm day}^{-1}$ , upward on the left, and downward on the right of background winds. These patterns are slightly weaker for cyclones due to asymmetries of the sea surface temperature composites.

We approximate eddy sea surface temperature patterns by a Gaussian

$$T(\mathbf{x}) = T_0 \exp\left(-\frac{\mathbf{x} \cdot \mathbf{x}}{2L^2}\right), \quad (22)$$

with amplitude  $T_0 = 1 \text{ K}$  and radius  $L = 70 \text{ km}$ . For background wind speed, we use a typical  $11 \text{ m s}^{-1}$ . The transfer function based reconstruction shows an increase of lee winds, or wind speed, of up to  $0.4 \text{ m s}^{-1}$  over the warm sea surface temperature, a dipole wind divergence with values of  $0.3 \times 10^{-5} \text{ s}^{-1}$  over the upwind and  $-0.6 \times 10^{-5} \text{ s}^{-1}$  over the downwind flanks of the sea surface temperature monopole (Figs. 5a,b). These values are consistent with results by Frenger et al. (2013) discussed above. The wind curl (Fig. 5c) displays the expected dipole over the crosswind flanks of the sea surface temperature monopole, with magnitudes weaker than those of the divergence, as suggested by smaller coupling coefficients (Chelton et al. 2004). The conversion of the wind curl to Ekman pumping involves linearizing the bulk formula for the wind stress  $\boldsymbol{\tau}$  around background winds (see appendix A and O'Neill et al. 2012):

$$\frac{\hat{\mathbf{e}}_3}{\rho f} \cdot (\nabla \times \boldsymbol{\tau}) = \rho_{\text{Air}} c_d U \{ (\hat{\mathbf{e}}_U \cdot \nabla) u_2 - 2 [ (\hat{\mathbf{e}}_3 \times \hat{\mathbf{e}}_U) \cdot \nabla ] u_1 \}, \quad (23)$$

where the neutral stability drag coefficient  $c_d$  is  $1.3 \times 10^{-3}$  for winds of  $U = 11 \text{ m s}^{-1}$  (Fairall et al. 2003), the air and seawater densities are  $\rho_{\text{Air}} = 1.2 \text{ kg m}^{-3}$  and  $\rho = 1023 \text{ kg m}^{-3}$ , respectively. The curl is dominated by lee wind component, so that the Ekman pumping

←

directions) in units of  $10^5 \text{ m}$ . Color shading in (a) shows the magnitude of the wind response. The sea surface temperature monopole is indicated by a black-and-white dashed circle in each panel.



pattern is very similar to that of the wind curl, and reaches values of  $8 \text{ cm day}^{-1}$ , similar to estimates by Gaube et al. (2015).

In addition to the increase of lee winds collocated with the warm monopole, the reconstruction (Fig. 5a) reveals positive port winds of  $0.15 \text{ m s}^{-1}$  that rotate wind vectors anticyclonically relative to background winds. Downwind, a wind wake has a marked asymmetry in the port direction. On the right side of the wake, winds retain speeds between  $0.15$  and  $0.1 \text{ m s}^{-1}$  and turn anticyclonic with increasing lee distance and reverse direction in just over  $300 \text{ km}$  from the sea surface temperature monopole. On the left side of the wake, winds are weaker, turn cyclonic, and form a spot of vanishing winds  $150 \text{ km}$  lee and  $50 \text{ km}$  port of the sea surface temperature monopole. As a result, the downwind wind convergence is enhanced, as found in composites from atmospheric model experiments (Foussard et al. 2019), and rotated to port compared to the upwind divergence (Fig. 5b). The anticyclonic pole of the wind curl extends into the downwind wake (Fig. 5c). To explore the governing processes, we turn to the transfer functions underlying the reconstruction.

### 5. Scale and Rossby number dependences

#### a. Winds

Wind transfer functions are shown in the plane of target lee and port wavenumbers for background wind speeds from  $1$  to  $21 \text{ m s}^{-1}$  in  $5 \text{ m s}^{-1}$  increments (Figs. 6a,f–e,j). For each target wavenumber and background wind speed, lee and port transfer functions are displayed as complex vectors  $(\hat{A}_1, \hat{A}_2) = \hat{e}_U \hat{A}_1 + \hat{e}_3 \times \hat{e}_U \hat{A}_2$ . Real parts  $\Re(\hat{A}_1, \hat{A}_2)$  capture lee and port winds in phase with warm sea surface temperatures (Figs. 6a–e). Imaginary parts  $\Im(\hat{A}_1, \hat{A}_2)$  describe winds that lag sea surface temperature by  $90^\circ$  (Figs. 6f–j) and are  $180^\circ$  out of phase with sea surface temperature gradients. Positive radial  $\mathbf{k}/|\mathbf{k}| \cdot \Im(\hat{A}_1, \hat{A}_2)$  and azimuthal  $(\hat{e}_3 \times \mathbf{k})/|\mathbf{k}| \cdot \Im(\hat{A}_1, \hat{A}_2)$  wind components are opposite to, and to the right of, the direction  $-i\mathbf{k}$  of sea surface temperature gradients, respectively.

Dynamical regimes in wavenumber space are distinguished by Rossby numbers  $U\hat{e}_U \cdot \mathbf{k}/|f|$ , where the Coriolis frequency  $f$  is evaluated at the center latitude of the study region. Unit Rossby number at lee wavenumbers  $\hat{e}_U \cdot \mathbf{k} = \pm|f|/U$  are marked in Fig. 6 with vertical dashed lines.

Overall, wind transfer function magnitudes recover published coupling coefficients (Fig. 6). Lee wind transfer functions have a positive real part on the order of  $0.5 \text{ m s}^{-1} \text{ K}^{-1}$ , consistent with reported coupling coefficients for the wind speed (O’Neill et al. 2010a,b).

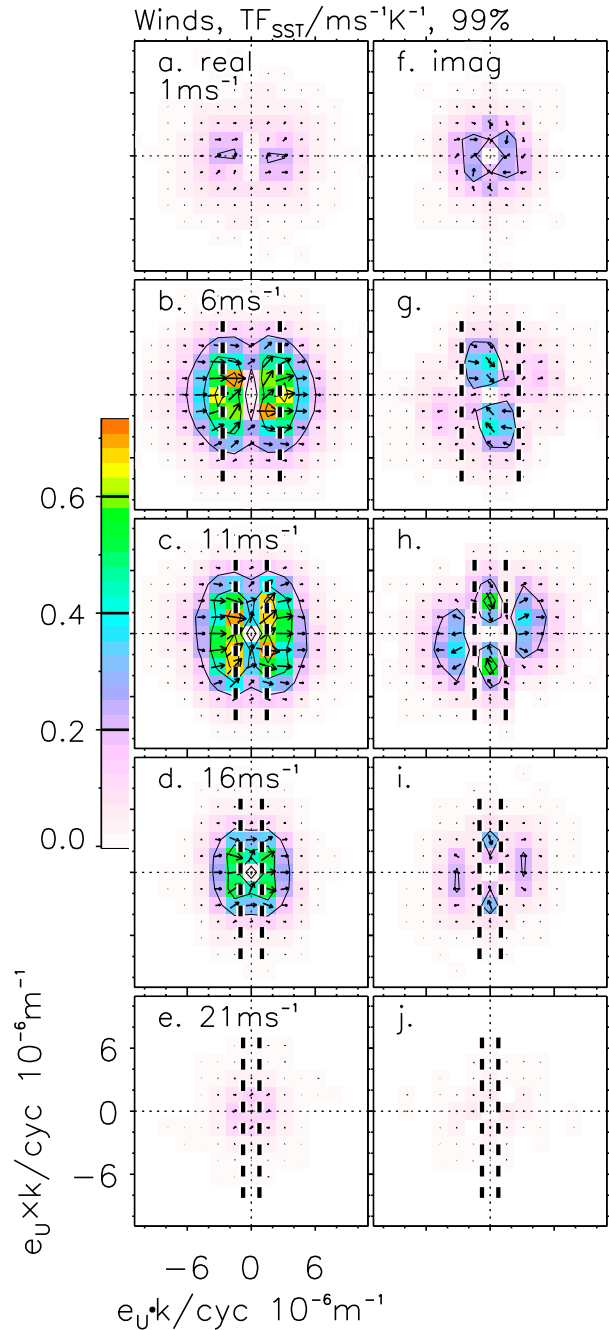


FIG. 6. (a)–(e) Real and (f)–(j) imaginary parts of wind transfer function ( $\text{m s}^{-1} \text{ K}^{-1}$ ). Rows show the transfer function for background wind speeds of (a),(f)  $1$ , (b),(g)  $6$ , (c),(h)  $11$ , (d),(i)  $16$ , and (e),(j)  $21 \text{ m s}^{-1}$ . Axes are lee and port wavenumbers in cycles per  $10^{-6} \text{ m}^{-1}$ . The transfer functions are shown as vectors, with components  $\hat{A}_1$  aligned with  $\hat{e}_U$ , and  $\hat{A}_2$  aligned with  $\hat{e}_3 \times \hat{e}_U$ , and magnitudes shown in color and contours (color scale on the left). Vertical dashed lines mark lee wavenumbers that correspond to unit Rossby number  $\hat{e}_U \cdot \mathbf{k}U/|f|$ . For background wind speeds of  $1 \text{ m s}^{-1}$  in (a) and (f), these wavenumber are outside of the range of abscissa values. Transfer functions are only shown when magnitudes exceed 99% confidence intervals.

Imaginary parts of  $\tilde{A}_2$  have values on the order of  $-0.3 \text{ m s}^{-1} \text{ K}^{-1}$  for positive port wavenumbers and a background wind of  $11 \text{ m s}^{-1}$ , and correspond to a cyclonic wind direction response of  $2^\circ \text{ K}^{-1}$ . Using the same data, O'Neill et al. (2010a) report similar results, with wind speeds increases of  $1\text{--}2 \text{ m s}^{-1}$  and cyclonic direction changes of  $4^\circ\text{--}8^\circ$  poleward of warm mesoscale sea surface temperature perturbations of  $2\text{--}4 \text{ K}$ . Cool sea surface temperatures elicit corresponding speed decreases and anticyclonic turning.

The wind transfer functions reveal a striking dependence on scale. They are anisotropic, attenuate toward high wavenumbers, and depend on the background wind speed. Rossby numbers separate different regimes. For background wind speeds of  $1 \text{ m s}^{-1}$ , real parts of transfer functions are small, and the imaginary parts form a clockwise, convergent pattern (Figs. 6a,f). For background winds of  $6 \text{ m s}^{-1}$ , real parts of the transfer function are largest at unit Rossby number (Fig. 6b), while imaginary parts are squeezed within the lee wavenumber range corresponding to Rossby numbers less than 1 (Fig. 6g). As background winds increase to  $11 \text{ m s}^{-1}$  real and imaginary peaks of the transfer functions shift to smaller lee wavenumber, consistent with the shift of unit Rossby numbers, and the imaginary part shows larger values for Rossby numbers larger than 1 (Figs. 6c,h). The scaling with Rossby number remains at  $16 \text{ m s}^{-1}$  background winds (Figs. 6d,i), while the magnitudes of the transfer function decrease. For the strongest background wind speed of  $21 \text{ m s}^{-1}$ , the wavenumber resolution is insufficient to resolve transfer function details, and magnitudes are small.

### 1) VERTICAL MIXING EFFECT

For Rossby numbers larger than 1, transfer functions are dominated by the lee component  $\tilde{A}_1$ , with prominent imaginary parts for lee wavenumbers beyond unit Rossby number. Focusing on background wind speeds of  $11 \text{ m s}^{-1}$ , real parts of the transfer functions reach values of up to  $0.6 \text{ m s}^{-1} \text{ K}^{-1}$  for lee wavenumbers of  $2.5 \times 10^{-6} \text{ cyc m}^{-1}$  (Fig. 6c), while port winds are small. Imaginary parts peak at  $0.3 \text{ m s}^{-1} \text{ K}^{-1}$  for lee wavenumbers  $4 \times 10^{-6} \text{ cyc m}^{-1}$  (Fig. 6h), and indicate maximum lee and port winds lagging warm sea surface temperatures.

These transfer functions are consistent with an advective balance and the dominance of the vertical mixing mechanism (Hayes et al. 1989; Wallace et al. 1989). The link between wind divergence and lee components of sea surface temperature gradients is commonly attributed to the vertical mixing effect (Chelton et al. 2001; O'Neill et al. 2003; Foussard et al. 2019). This is consistent with enhancements of  $\tilde{A}_1$  contributions to the wind divergence at large lee wavenumbers in Eq. (13),

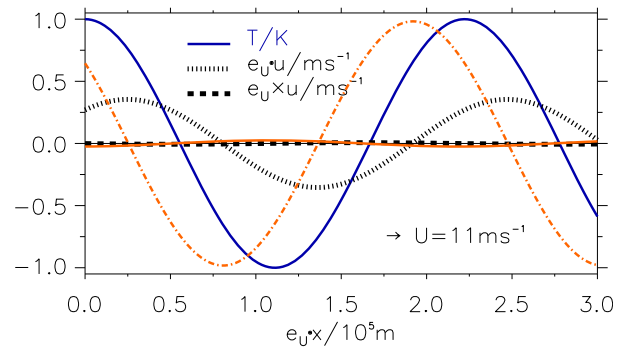


FIG. 7. Response of lee (black dotted) and port (black dashed) wind components ( $\text{m s}^{-1}$ ) to a sinusoidal sea surface temperature (blue) with an amplitude of  $1 \text{ K}$ . The port wavenumber is 0. The lee wavenumber of  $0.45 \times 10^{-5} \text{ m}^{-1}$  and a background wind blowing toward the right across contours of sea surface temperature with speeds of  $11 \text{ m s}^{-1}$  correspond to a Rossby number of 3 at a latitude  $45^\circ \text{S}$ . Red lines mark wind divergence (dash-dotted) and curl (solid), both in units of  $10^{-5} \text{ s}^{-1}$ .

and with the scaling discussed in the introduction that the vertical mixing mechanism dominates at large Rossby number. We therefore attribute positive real parts of  $\tilde{A}_1$  at large Rossby numbers to the vertical mixing effect.

To illustrate, we reconstruct from the transfer function the physical space wind response to a single Fourier component of sea surface temperature at a Rossby number of 3. The corresponding lee wavenumber is  $4.5 \times 10^{-6} \text{ cyc m}^{-1}$ , the port wavenumber vanishes, and the sea surface temperature amplitude is  $1 \text{ K}$ . Lee winds increase by  $0.3\text{--}0.4 \text{ m s}^{-1}$  with the maximum response shifted about  $2.5 \times 10^6 \text{ m}$  in the downwind direction from warm sea surface temperatures (Fig. 7). Winds capture the positive correlations of mesoscale sea surface temperatures and wind speeds and of wind divergence and the lee gradient of sea surface temperatures. Port winds are small, and suggest nonrotating physics. The large Rossby number, the lagged responses, and the collocation of the wind divergence and the lee component of sea surface temperature gradient suggest a balance of advection with the vertical mixing effect (Hayes et al. 1989; Wallace et al. 1989), with rotation being unimportant.

### 2) EKMAN DYNAMICS

For Rossby numbers smaller than 1, transfer functions have very different scale dependences (Fig. 6). At background wind speeds of  $11 \text{ m s}^{-1}$  imaginary parts of transfer functions for lee and port winds reach values of  $0.4$  and  $0.3 \text{ m s}^{-1} \text{ K}^{-1}$ , respectively (Fig. 6h), and increase linearly with the port wavenumber from the origin to  $0.3 \times 10^{-5} \text{ cyc m}^{-1}$ . As background winds decrease to  $6 \text{ m s}^{-1}$ , the low Rossby number range expands and

is better resolved (Figs. 6b,g) and encompasses, at  $1 \text{ m s}^{-1}$ , the entire wavenumber domain considered (Figs. 6a,f).

In the small lee-wavenumber and Rossby number regime,  $\mathfrak{J}(\tilde{A}_1, \tilde{A}_2)$  spiral clockwise toward the origin of wavenumber space, that is, in direction and to the left of the sea surface temperature gradient. Magnitudes of imaginary parts of  $\tilde{A}_1$  and  $\tilde{A}_2$  increase approximately linearly with the wavenumber magnitude for the lowest three wavenumbers and suggest that the wind divergence and curl are proportional to the Laplacian of sea surface temperature.

These directional and wavenumber dependences of the imaginary parts of the surface wind transfer functions are consistent with responses of an Ekman layer to the pressure effect, that is, to reduced sea surface pressure due to warm, ocean-mesoscale, sea surface temperatures (Feliks et al. 2004; Minobe et al. 2008; Lambaerts et al. 2013). For winds of  $6 \text{ m s}^{-1}$  and stronger, Ekman dynamics are active primarily in the port direction (O'Neill et al. 2010b; Foussard et al. 2019) since lee wavenumbers are limited to small Rossby numbers.

Real parts of the transfer function are nonzero, and sport asymmetries about the lee wavenumber axis. At  $6 \text{ m s}^{-1}$  lee wind transfer functions reach  $0.6 \text{ m s}^{-1} \text{ K}^{-1}$  in the upper-left sector of positive port and negative lee wavenumbers (Figs. 6b,c), while port winds attain values to  $0.4 \text{ m s}^{-1} \text{ K}^{-1}$  in the upper-right sector for positive lee wavenumbers (Figs. 6b,c). The increase of these terms toward unit Rossby number suggests that advection and the vertical mixing play roles.

To demonstrate the underlying physics, the response in physical space to a sharp sea surface temperature front is reconstructed based on the transfer functions. Background winds of  $6 \text{ m s}^{-1}$  blow along a  $2 \text{ K}$  sea surface temperature front with warm waters on the left. Variations in alongfront and background wind directions vanish so that the lee wave and Rossby numbers are 0. Reconstructed winds are smoother than the sharp sea surface temperature front (Fig. 8) since transfer functions attenuate toward high wavenumbers and act as a low pass filter. For the zero Rossby numbers considered, sea surface temperatures imprint on boundary layer temperatures and hydrostatic pressure, with warm (cold) waters associated with low (high) pressure. Accordingly, winds consist of a cross-frontal sea breeze from cold to warm waters, and an alongfront wind jet with the warm water on the right, consistent in direction with Southern Hemisphere geostrophy (Fig. 8). Wind divergence and curl form dipoles with positive values of  $0.5 \times 10^{-5}$  and  $0.4 \times 10^{-5} \text{ s}^{-1}$ , respectively, on the cold side of the front, consistent with a low-pass filtered response to the Laplacian of sea surface temperature.

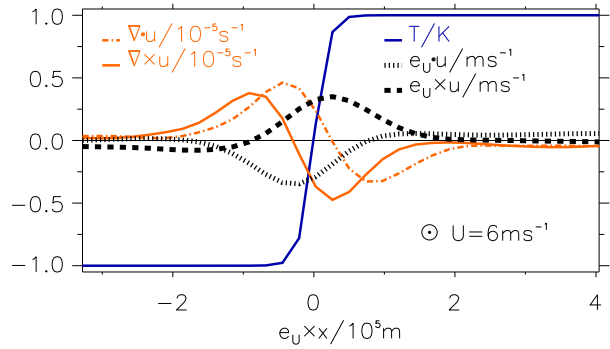


FIG. 8. Zero Rossby number wind response ( $\text{m s}^{-1}$ ) to a sharp sea surface temperature front. Sea surface temperatures are cool on the left and warm on right (blue solid line, K). Background winds blow along the front at  $6 \text{ m s}^{-1}$  with  $\hat{e}_U$  pointing out of the page. Port winds are shown in black and dashed; positive values indicate winds that cross the front toward warm waters. Lee winds are shown with a black dotted line. Negative lee winds oppose background winds, as is a geostrophic wind in response to low (high) pressure over warm (cool) waters. Red lines mark wind divergence (dash-dotted) and curl (solid), both in units of  $10^{-5} \text{ s}^{-1}$ .

These wind responses suggest a modulation of the bottom Ekman layer by sea surface temperature-induced hydrostatic pressure gradients in the atmospheric boundary layer.

The real parts of the transfer function (Figs. 6a–c) move wind responses off the front. The shifts are independent of the sign of the across-front sea surface temperature gradient, to the left of the background winds for sea breeze and divergence, to the right for alongfront jet and wind curl (Fig. 8), and increase for background winds of  $11 \text{ m s}^{-1}$ . This likely results from spectral resolution and the asymmetry of the transfer functions about the port wavenumber axis: The real parts of transfer functions nearly vanish for zero lee wavenumbers and background winds of  $1 \text{ m s}^{-1}$  (Fig. 6a). As background wind speeds increase to 6 and  $11 \text{ m s}^{-1}$ , small Rossby numbers are compressed into narrow band of lee wavenumbers that, for the spectral resolution of the analysis, smooth this transfer function minimum and yield a non-zero real values (Figs. 6b,c).

### 3) NEAR-INERTIAL LEE WAVE IN RESPONSE TO VERTICAL MIXING AND PRESSURE EFFECTS

Rossby numbers of order 1 bring together advection, Coriolis acceleration, vertical mixing, and pressure gradients. To explore these dynamics, we return to the example of wind response to a sea surface temperature monopole, Eq. (22), that excites all wavenumbers smaller than  $L^{-1} = 1.33 \times 10^{-5} \text{ cyc m}^{-1}$  (Fig. 5a). Over the warm sea surface temperature, positive lee and port winds are consistent with increased vertical mixing in the presence of anticyclonic background wind shear between the frictionally

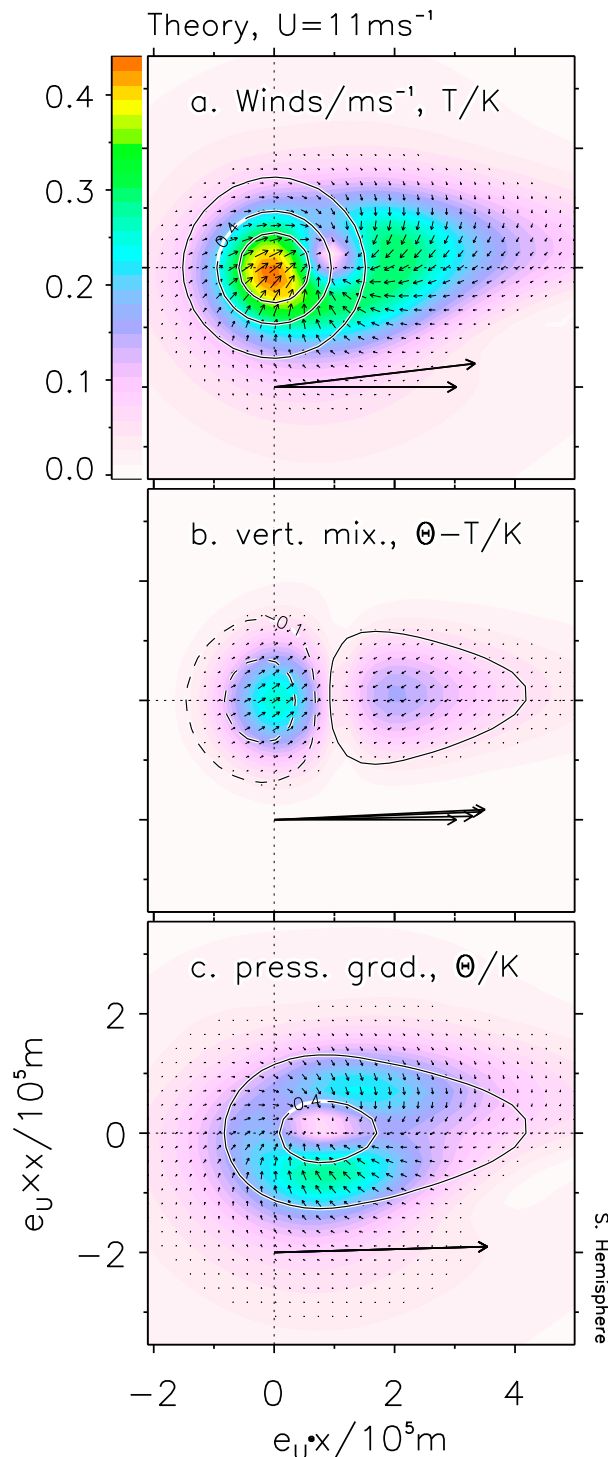


FIG. 9. Surface wind responses (small arrows) based on the linear theory Schneider and Qiu (2015) to a Gaussian sea surface temperature monopole with an amplitude of 1 K in the Southern Hemisphere. (a) Total winds are split into contributions due to (b) vertical mixing and (c) pressure effects. Arrows represent displacements during an inertial period. Wind magnitudes ( $\text{m s}^{-1}$ ) are displayed by colors with scale on upper left. Background surface winds blow to the right with a magnitude of  $11 \text{ m s}^{-1}$  and are shown

influenced surface to the geostrophic regime aloft in the bottom Ekman layer. To the lee of the monopole, winds rotate in an anticyclonic direction with a half wavelength that matches  $\pi U/|f|$  of 336 km for background a wind speed of  $11 \text{ m s}^{-1}$  and a latitude of  $45^\circ$ . This indicates the excitation of near-inertial lee waves (Spall 2007; O'Neill et al. 2010b; Kilpatrick et al. 2014). The asymmetry in port direction suggests that the pressure effect exerts a force into the warm wake in the lee of the sea surface temperature monopole that enhances the vertical mixing effect and inertial turning of winds on the right side of the wake, but destructively interferes on its left side.

To test this physical scenario, we turn to the theory of Schneider and Qiu (2015), summarized in appendix B, and its response to the sea surface temperature monopole of Eq. (22) for an  $11 \text{ m s}^{-1}$  surface background wind in the Southern Hemisphere. Wind reconstructions based on the theory (Fig. 9a) capture major aspects of the observationally based patterns (Fig. 5). Winds increase by  $0.4 \text{ m s}^{-1}$  and turn anticyclonically over the warm sea surface temperature monopole. To the lee of the monopole, winds form an asymmetric wake with larger speeds and anticyclonic turning on the right flank, and a local minima about 100 km downwind from the origin on the left flank. Wind direction reverses 200–300 km downwind of monopole. Winds in the wake predicted by theory reach  $0.3 \text{ m s}^{-1}$  and extend 300–400 km in the lee direction, stronger than in observational reconstruction with speeds of less than  $0.2 \text{ m s}^{-1}$  and an extent of less than 300 km.

The impacts of vertical mixing and pressure effects are separated by solutions to their respective components of  $\mathbf{F}$  in Eq. (2) alone. The vertical mixing effect leads to a collocated increase in lee and port winds (Fig. 9b, small arrows and color shading), consistent with increases of mixing over negative air–sea temperature differences (Fig. 9b, dashed contour) that act on anticyclonic background shear (Fig. 9b, heavy arrows). The warm wake extends to  $2U/\gamma = 3.7 \times 10^5 \text{ m}$  beyond the sea surface temperature monopole (Fig. 9c, contours) so that positive air–sea temperature differences centered around

←

as large, thick arrows including (a) prescribed geostrophic wind to the left of surface winds, (b) the Ekman spiral with anticyclonic turning of winds from the surface to the inversion, and (c) the vertical average of the Ekman spiral. Background wind arrows are displacements during (a),(b) half an inertial period and (c) two thermal damping time scales. Contours show (a) sea surface temperature, (b) air–sea temperature difference, and (c) air temperature in K. Contour levels are  $\pm 0.1, 0.4, 0.7$ , with negative values denoted by dashed lines.

$2 \times 10^5$  m reduce mixing and accelerate winds opposite to background shear. Scales of the wind response due to the vertical mixing effect mirror those of the sea surface temperature monopole and the resulting air–sea temperature differences.

In contrast, winds due to the pressure effect have scales in the lee direction that are larger than the sea surface temperature monopole and are commensurate with the lee wake of warmed air (Fig. 9c, small arrows and contours). Winds match the scale of the monopole in the port direction and are largest on the flanks of the wake. The dominance of the pressure gradient force in  $(\hat{e}_3 \times \hat{e}_U) \cdot \mathbf{F}$  and the port momentum equations (O’Neill et al. 2010b; Foussard et al. 2019) is evident. Since lee scales of thermal and inertial wakes  $\pi U/|f| = 3.4 \times 10^5$  m match, the Coriolis force imparts an anticyclonic acceleration and forms a Doppler-shifted near-inertial lee wave (Spall 2007; O’Neill et al. 2010b; Kilpatrick et al. 2014). On the right side of the wake, pressure gradient forces, vertical mixing effect, and inertial turning constructively interfere and enhance the response compared to the left side of the wake, where the interferences are destructive.

*b. Wind divergence and curl*

Wind divergence and curl transfer functions  $\tilde{A}_3$  and  $\tilde{A}_4$  are estimated from  $\tilde{A}_1$  and  $\tilde{A}_2$  via their definitions (13) and (14). Magnitudes of transfer functions of wind divergence lie between  $0.5 \times 10^{-5}$  to  $1 \times 10^{-5} \text{ s}^{-1} \text{ K}^{-1}$  (Fig. 10) and are approximately a factor of 2 larger than those of the wind curl (Fig. 11), consistent with the ratio of coupling coefficients (Chelton et al. 2004; O’Neill et al. 2010a). Imaginary parts dominate and reflect the impact of  $\tilde{A}_1$  multiplied with the lee (port) wavenumbers in the calculation of wind divergence (curl) in Eqs. (13) and (14). They are largest in lee- (port-) wavenumber direction, consistent with the dependence of divergence (curl) on the lee (port) components of the sea surface temperature gradients (e.g., Chelton et al. 2004).

As for wind components, Rossby numbers delineate dynamical regimes. For Rossby numbers large compared to 1, divergence transfer functions are dominated by imaginary parts (Figs. 10g–i) with weaker real parts (Figs. 10b–d) that are roughly symmetric about the lee-wavenumber axis. For port wavenumbers near 0, the wind curl is small (Fig. 11). This is the situation depicted in wind response to a single Fourier component of sea surface temperature at a Rossby number of 3 (Fig. 7).

As the Rossby number is reduced and approaches 1, the amplitudes of imaginary and real parts of wind divergence and curl transfer functions increase and become asymmetric about the lee-wavenumber axis

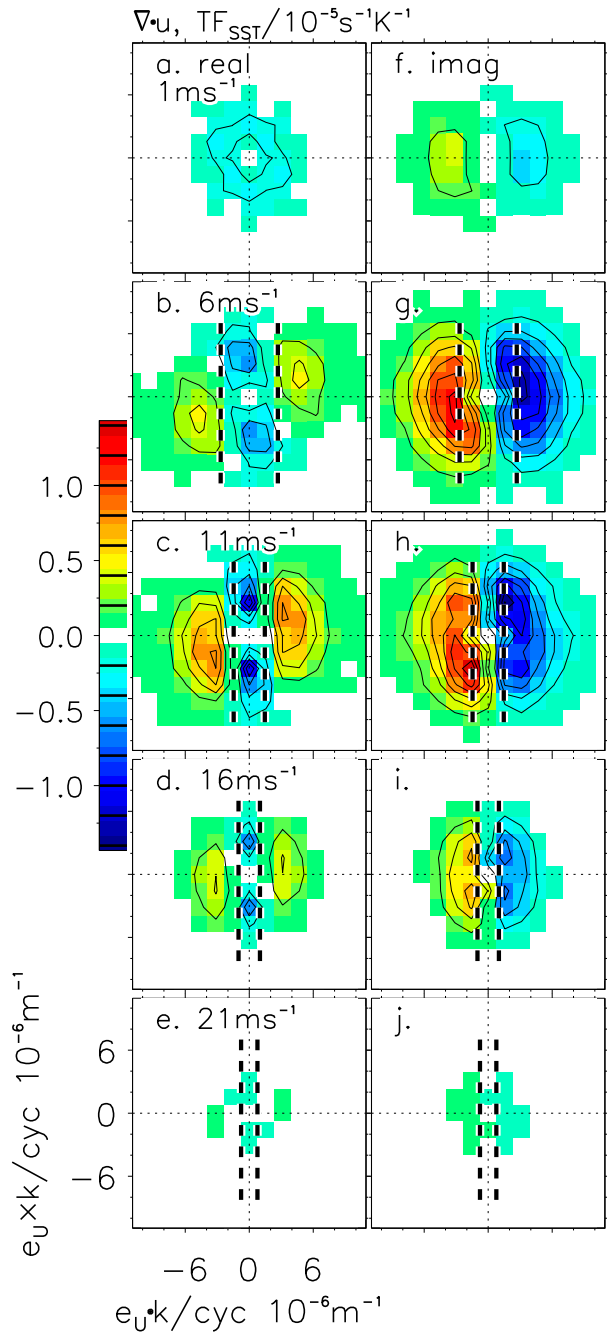


FIG. 10. As in Fig. 6, but for the transfer function of the wind divergence ( $10^{-5} \text{ s}^{-1} \text{ K}^{-1}$ , color scale on the left).

(e.g., Figs. 10 and 11c,h). Divergence transfer functions are larger for wavenumbers to the left of background winds, while the curl is larger for wavenumber to the right of background winds. This underlies the stronger wind divergence to the left (Fig. 5b), and the stronger wind curl to the right of background winds (Fig. 5c) in the response to the sea surface temperature monopole.

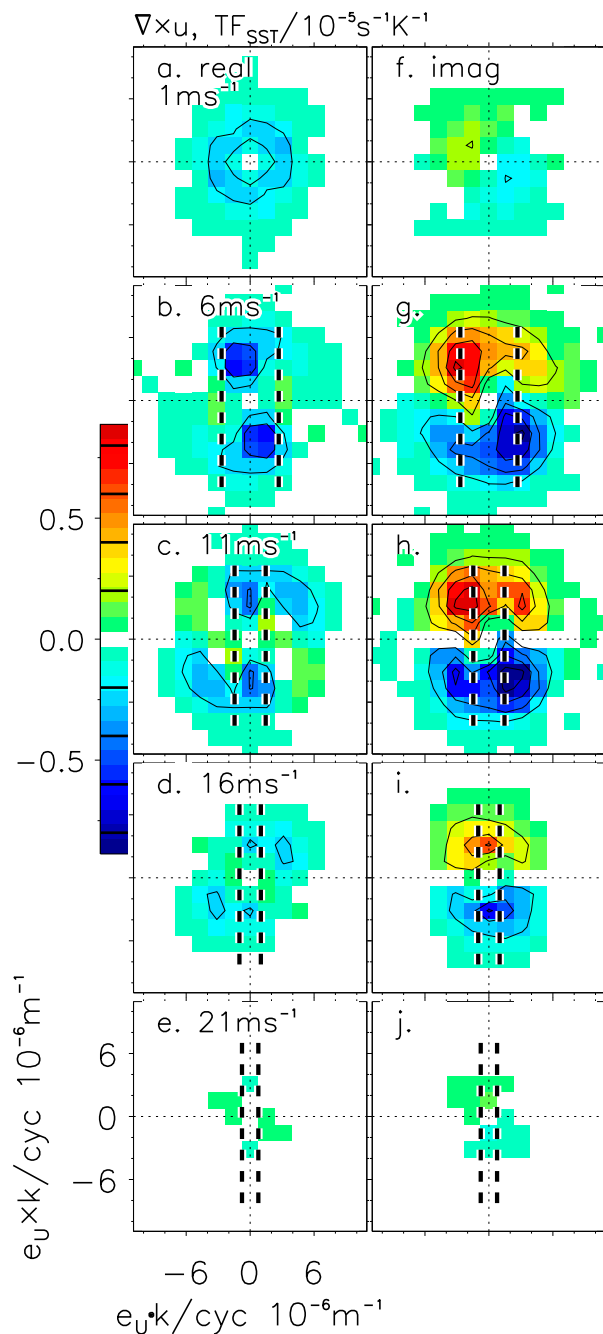


FIG. 11. As in Fig. 10, but for the transfer function of the wind curl ( $10^{-5} \text{ s}^{-1} \text{ K}^{-1}$ ).

For Rossby numbers smaller than 1, real parts of wind divergence and curl transfer functions are negative, and are, for low port wavenumber magnitudes, consistent with the spectral  $-\mathbf{k} \cdot \mathbf{k}$  dependence expected from the Laplacian of sea surface temperature and an Ekman response to the imprint of sea surface temperature on boundary layer hydrostatic pressure (Feliks et al. 2004;

Minobe et al. 2008; Lambaerts et al. 2013). This is best seen for background wind speeds of  $1 \text{ m s}^{-1}$ . Real parts of divergence (Fig. 10a) and curl (Fig. 11a) are negative, and suggest cyclonic and convergent circulations over warm sea surface temperature perturbations. Note, however, that this dependence is limited to the lowest few wavenumbers, for higher wavenumbers transfer functions decay.

## 6. Fundamental wind response patterns

In physical space, impulse response functions  $A_j$ ,  $j = 1, \dots, 4$ , defined in Eq. (15), are the fundamental wind patterns excited by ocean-mesoscale sea surface temperature, and are obtained from satellite observed transfer functions via Eq. (16). Figure 12 shows wind impulse response functions for a sea surface temperature impulse of  $1 \text{ K m}^2$  that corresponds to a  $1\text{-K}$  sea surface temperature perturbation over an area of  $1 \text{ m}^2$  condensed into a Dirac delta function.

For the lowest background wind speed of  $1 \text{ m s}^{-1}$  the combination of lee and port wind impulse response functions form a cyclonic circulation that converges toward the origin (Fig. 12a), with negative wind divergence and curl (Figs. 13a,e). This is consistent with the response of the bottom Ekman layer to low hydrostatic pressure induced by the warm surface waters.

Stronger background winds of 6 and  $11 \text{ m s}^{-1}$  yield wind impulse response functions with spatial footprints of 100 km in the up- and crosswind, and 200–250 km in the downwind directions (Figs. 12b,c), with stronger background winds extending the wake. Patterns and physical interpretation of impulse response functions are similar to the wind responses to a Gaussian sea surface temperature monopole (Fig. 5), because transfer functions decay toward high wavenumbers (Fig. 6) and act as a low-pass filter, and because a Gaussian of unit volume becomes a Dirac delta functions in the limit of zero radial scale and concomitant infinite amplitude. Impulse response functions are dominated by the lee wind component just downwind of the origin, with a magnitude of up to  $0.5 \times 10^{-10} \text{ m}^{-1} \text{ s}^{-1} \text{ K}^{-1}$ . On the left side of wake, magnitudes are weak, turn cyclonically and form a local minimum 75 and 100 km downwind of the origin. On the right side of the wake, winds have magnitudes of  $0.2 \times 10^{-10} \text{ m}^{-1} \text{ s}^{-1} \text{ K}^{-1}$ , turn anticyclonically, and form a local maximum about 120 to 150 km downwind of the origin (Figs. 12b,c). About 200 to 220 km downwind of the origin, the turning leads to a reversal of the wind direction, and the response decays. As the background winds increase to  $16 \text{ m s}^{-1}$  the response weakens, and the downwind reversal of near-inertial lee wave occurs

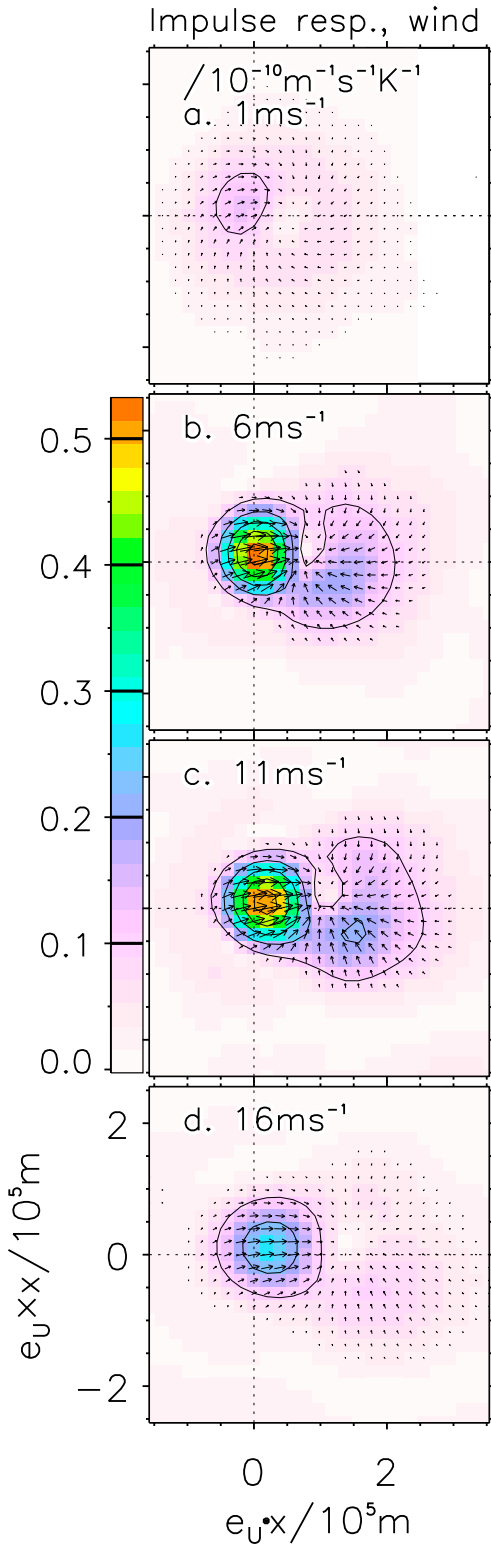


FIG. 12. Impulse response function for winds ( $10^{-10} \text{ m}^{-1} \text{ s}^{-1} \text{ K}^{-1}$ ) as a function of lee and port lags ( $10^5 \text{ m}$ ) and for background wind speeds from (a) 1 to (d)  $16 \text{ m s}^{-1}$  in increments of  $5 \text{ m s}^{-1}$ . The response at  $21 \text{ m s}^{-1}$  is insignificant and not shown. Colors denote the magnitudes and correspond to the scale on the left.

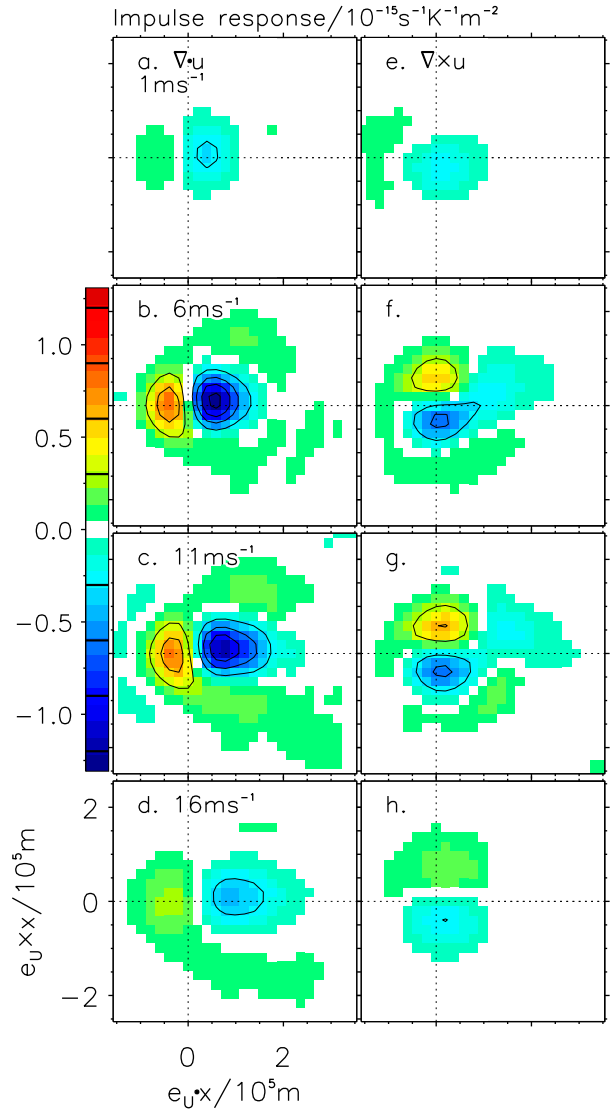


FIG. 13. As in Fig. 12, but for (a)–(d) wind divergence and (e)–(h) wind curl, both in units of  $10^{-15} \text{ s}^{-1} \text{ K}^{-1} \text{ m}^{-2}$ .

farther downstream (Fig. 12d). For the strongest winds of  $21 \text{ m s}^{-1}$  the response is very weak, and barely discernible (not shown).

Impulse response functions for wind divergence (Figs. 13a,d) and curl (Figs. 13e,h) show downwind and crosswind dipoles, respectively, with notable asymmetries. For background winds of 6 and  $11 \text{ m s}^{-1}$ , wind divergences are positive with values of  $0.6 \times 10^{-15} \text{ s}^{-1} \text{ K}^{-1} \text{ m}^{-2}$  on the upwind, and negative and stronger with values of  $-0.9 \times 10^{-15} \text{ s}^{-1} \text{ K}^{-1} \text{ m}^{-2}$  on the downwind pole that is shifted to the left of the wake, and flanked by weakly positive values (Figs. 13b,c). The wind curl is positive (cyclonic) with values of  $0.6 \times 10^{-15} \text{ s}^{-1} \text{ K}^{-1} \text{ m}^{-2}$  to the left, and negative (anticyclonic) and stronger to the

right of background winds that extends downwind the dominant negative lobe through the center of the wake and to its left (Figs. 13f,g). For background winds of  $16 \text{ m s}^{-1}$  responses weaken (Figs. 13d,h).

These impulse response functions reiterate the physical scenario seen in the response to a sea surface temperature monopole. Warm mesoscale sea surface temperatures decrease boundary layer stability, locally increase vertical mixing, and force a downwind wake of warmer air and reduced hydrostatic pressure. This excites Doppler-shifted near-inertial lee waves that interfere constructively with the pressure gradient forces and vertical mixing on the right side of the wake, while destructive interference diminishes wind responses on the left side. The extent of the downstream wake does not scale linearly with background wind speeds since the physical space response juxtaposes scale dependent responses, as given by the transfer functions (Fig. 6), and combines distinct nonadvective and advective physics. The interference pattern in the wake depends on a match between near-inertial time scales and the thermal adjustment time scales of the boundary layer and is likely affected by boundary layer height and background wind speeds. For strongest winds, the reduction of the impulse response function suggests a possible mismatch, diminished influence of sea surface temperature relative to

background winds, insufficient spectral resolution of the transfer functions, or damping of the detected signal as the length scale of the inertial wake of  $\pi U/|f|$  approaches the diameter of the analysis stencil used in the least squares fitting procedure.

## 7. Impact of averaging

Published estimates of the wind responses to sea surface temperature perturbations associated with eddies and ocean fronts identify collocations of warm mesoscale sea surface temperatures and increases of lee winds, and of lee (port) components of sea surface temperature gradients and wind divergences (curl) (e.g., Chelton et al. 2004; Chelton and Xie 2010; O'Neill et al. 2010a; Frenger et al. 2013), but do not report the downwind lagged structures and asymmetries of winds, wind curl and divergences discussed here (Figs. 12 and 13) and found in an atmospheric simulation (Foussard et al. 2019). Here, we suggest that time averages deployed to filter atmospheric synoptic variability diminishes lagged signals, and document that reconstructions using averaged transfer functions recover published results.

Averaged wind responses to steady sea surface temperature features in Eq. (15) accumulate impulse response functions for all occurring background winds

$$\bar{A}_j[\bar{\mathbf{e}}_u \cdot \mathbf{x}, (\hat{\mathbf{e}}_3 \times \bar{\mathbf{e}}_u) \cdot \mathbf{x}] = \int d\hat{\mathbf{e}}'_U dU A_j\{(\bar{\mathbf{e}}_u + \hat{\mathbf{e}}'_U) \cdot \mathbf{x}, [\hat{\mathbf{e}}_3 \times (\bar{\mathbf{e}}_u + \hat{\mathbf{e}}'_U)] \cdot \mathbf{x}, U\} f(\hat{\mathbf{e}}'_U, U), \quad j=1, \dots, 4, \quad (24)$$

with equivalent formulations for the averaged transfer function  $\bar{A}_j(\mathbf{x})$  in Eq. (12). An overbar denotes averages, primes deviations thereof, and we integrate over all background wind speeds. The characteristics of the joint distribution of background wind direction and speeds  $f(\hat{\mathbf{e}}'_U, U)$  determine the smoothing of the transfer and impulse response functions. If the distribution is symmetric about the origin, the imaginary part of the transfer function and lagged components of the impulse response function vanish, and averaging emphasizes the in-phase responses. If the distribution is sharply peaked,  $\bar{A}_j$  are similar to  $A_j$  evaluated at the mean values of  $\hat{\mathbf{e}}_U$  and  $U$ .

To show the impact on transfer and impulse response functions, we average wind direction over seven days as in Frenger et al. (2013). Extending the averaging interval to all realizations reduces the impulse response functions by about 10%–20% compared to the seven day averages, with little additional impact on the patterns. Averaged impulse response functions are estimated by

randomly selecting 800 realizations, determining for each the deviations from the average background wind directions of the preceding and following three days, and integrating over impulse response functions in the coordinate system aligned with the 7-day averaged background wind directions. Note, however, that lee and port wind components remain defined relative to daily winds, as is the averaging of instantaneous speed (e.g., Chelton et al. 2004; Frenger et al. 2013).

In the Southern Ocean study region, daily background winds have broad distributions of direction and speed about mean westerlies with an average speed of  $8 \text{ m s}^{-1}$  (Fig. 3). Seven-day averages of background winds remove the majority of atmospheric synoptic variability (Frenger et al. 2013), with 65% of the averaged background winds occupy the westerly and west-north westerly sectors, and 20% the surrounding west-southwesterly and northwesterly sectors.

Averaged impulse response functions recover the increase of lee winds collocated with high sea surface



temperatures, and the dipoles of wind divergence and wind curl that straddle the warm waters, albeit with reduced magnitudes. Averages drastically reduce lagged wind signals. Averaged wind impulse response functions show positive lee winds of  $0.4 \times 10^{-10} \text{ m}^{-1} \text{ s}^{-1} \text{ K}^{-1}$  colocated and slightly downwind of warm sea surface temperature at the origin (Fig. 14a), smaller than the instantaneous values of  $0.5 \times 10^{-10} \text{ m}^{-1} \text{ s}^{-1} \text{ K}^{-1}$  (Figs. 12b,c) and reduce to barely perceptible values the downstream near-inertial lee wave (Fig. 14a). For the wind divergence, averaged impulse response function retain the dipole structure, with upstream positive values of up to  $0.5 \times 10^{-15} \text{ s}^{-1} \text{ K}^{-1} \text{ m}^{-2}$  and a downwind pole of  $-0.6 \times 10^{-15} \text{ s}^{-1} \text{ K}^{-1} \text{ m}^{-2}$  (Fig. 14b). However, the downwind extent and asymmetry are reduced compared to instantaneous impulse response functions with up- and downwind values of  $0.6 \times 10^{-15}$  and  $-1.1 \times 10^{-15} \text{ s}^{-1} \text{ K}^{-1} \text{ m}^{-2}$ , respectively (Figs. 13b,c). Similarly, the average wind curl impulse response function retains its crosswind dipole (Fig. 14c), but with an amplitude reduced by a third (Figs. 13f,g), and a much reduced downwind anticyclonic wake of less than  $0.1 \times 10^{-15} \text{ s}^{-1} \text{ K}^{-1} \text{ m}^{-2}$ .

**8. Conclusions**

Motivated by linear theory (Schneider and Qiu 2015), this contribution explores the covariability of observed mesoscale sea surface temperatures and surface winds using transfer and impulse response functions that capture scale dependences and lagged signals. Transfer and impulse response functions are fundamental wind-response patterns in spectral and physical spaces, respectively, and are constrained by, and allow reconstructions of, wind responses to any mesoscale sea surface temperature patterns, including ocean eddies, fronts, and meanders.

Transfer functions of wind components aligned with and perpendicular to the left of the large-scale winds, dubbed “lee” and “port,” are estimated as a function of lee and port wavenumbers and background wind speeds from daily AMSR-E radiometer sea surface temperatures and QuikSCAT scatterometer equivalent neutral winds. The study area is the Agulhas Return Current in the Southern Ocean for the years 2003 to 2008. Cross-validated wind reconstructions using the transfer functions have high skill, and suggest a physical grounding of the approach.

Transfer functions for lee and port wind components, wind divergence and wind curl recover published coupling coefficients, and reveal a strong dependence on spatial scale and Rossby number. For Rossby numbers large compared to 1, lee winds include in-phase and lagged components, while port winds are small, and indicate a

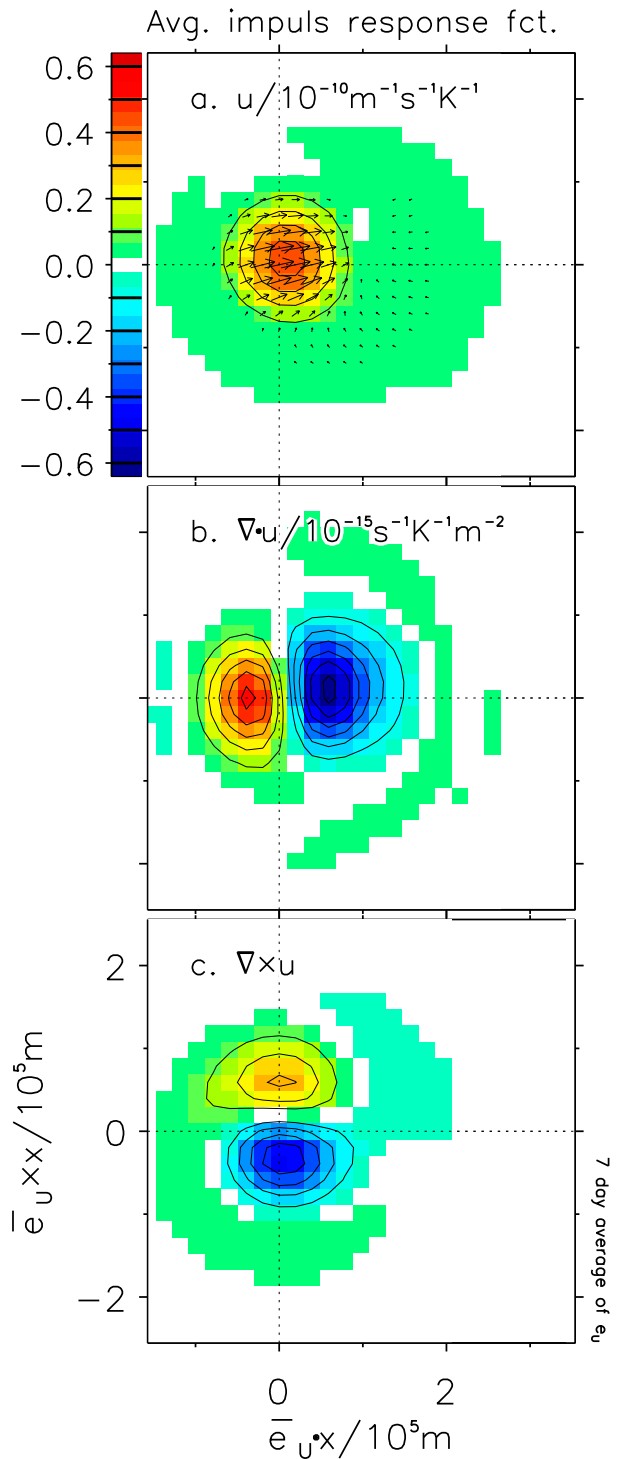


FIG. 14. Averaged impulse response functions for (a) winds ( $10^{-10} \text{ m}^{-1} \text{ s}^{-1} \text{ K}^{-1}$ ) and (b) wind divergence and (c) wind curl, both in units of  $10^{-15} \text{ s}^{-1} \text{ K}^{-1} \text{ m}^{-2}$ . Averages have been performed over 7 days for background wind direction and over all background wind speeds. The abscissa and ordinates are distances in direction and perpendicular to the 7-day averaged background wind direction. Note that vectors of lee and port winds are relative to the instantaneous and not to the time-averaged background winds.

balance of advection and modulation of vertical mixing in the boundary layer induced by ocean-mesoscale sea surface temperatures (O'Neill et al. 2010b). Wind divergences are largest in the downwind direction and are phase shifted with respect to sea surface temperature, consistent with reported relations with the downwind sea surface temperature gradient. The wind curl response is smaller than the divergence.

For Rossby numbers small to 1, lee and port wind responses indicate the surface expressions of a solenoidal circulation akin to a sea breeze and of a geostrophic winds, and are consistent with the response of a bottom Ekman layer to the ocean-mesoscale-induced hydrostatic pressure fluctuations (Lindzen and Nigam 1987). Accordingly, wind divergence and curl match the Laplacian of sea surface temperature (Feliks et al. 2004; Minobe et al. 2008; Lambaerts et al. 2013).

For Rossby numbers of order 1, transfer function are largest and combine vertical mixing and pressure effects with advection and rotation. The response to all Rossby numbers is viewed in physical space by impulse response functions, the inverse Fourier transform of transfer functions. Over warm sea surface temperatures, air-sea heat exchanges destabilize the boundary layer, heat the air and lead to a warm downwind wake with a scale commensurate with a near-inertial lee wave. Enhanced vertical mixing over warm waters accelerates surface winds in direction of background winds aloft. Due to interactions of pressure gradient, modulation of vertical mixing and Coriolis forces, wind responses on the right flank of the wake are enhanced. As air moves with the background winds, hydrostatic pressure gradient forces into the warm wake turn anticyclonically on the right side of the wake, in phase with inertial turning and the vertical mixing effect. On the left side, pressure gradient forces turn cyclonically and opposite to inertial accelerations and vertical mixing. Wind divergences form a dipole in the direction of background winds, with a stronger downwind pole. The wind curl is smaller than the wind divergence, and feature a dipole across background winds, with anticyclonic values to the right of the warm sea surface temperature perturbation that extend into the downstream wake.

In addition to the dependence on the Rossby number, wind responses are modulated directly by background wind speed and wavenumber magnitudes. Transfer functions are small for background winds close to 0 and maximum for winds around  $11 \text{ m s}^{-1}$  and are reduced toward the higher background wind speeds. Transfer functions decay for wavenumber magnitudes larger than  $0.5 \times 10^{-5} \text{ cyc m}^{-1}$  and are 0 for wavenumber magnitudes beyond  $0.75 \times 10^{-5} \text{ cyc m}^{-1}$ . These results may be artifacts

of the analysis footprint and spectral leakage, or may reflect physical processes.

For strong background winds, the spatial area deployed to estimate transfer functions fails to reach all upstream sea surface temperatures, reducing the estimate. For background winds of  $16 \text{ m s}^{-1}$  and stronger, the distance traveled during half an inertial period of 500 km exceeds the lag in longitude of at most 470 km between the  $8^\circ$  square stencil of the sea surface temperature region and the inner  $4^\circ$  square region for winds. Alternatively, weak responses at high wind speeds may be associated with stronger mixing and deeper boundary layers that overwhelm perturbations due to ocean-mesoscale sea surface temperatures.

Diminished transfer functions at high wavenumber may result from the use of a single background wind for all wavenumbers that excludes the impact of low wavenumbers winds on the lee and port directions for high wavenumbers, or may reflect the importance of the local rate of change including lags in the adjustment of vertical mixing (Wenegrat and Arthur 2018). For high wavenumbers, natural frequencies in the gravity wave regime larger than  $f$  and  $\gamma$  are not resolved by the twice daily wind observations and moot the steady-state assumption of the wind response to sea surface temperatures. New, high-resolution sensors and processing, as well as analysis of high-resolution numerical models, will reveal the processes and coupling of sea surface temperatures and surface winds at strong background winds and scales smaller than 100 km.

Wind reconstructions based on the theory (Schneider and Qiu 2015) capture major aspects of reconstructions from observed transfer functions and support their dynamical interpretation. Specifically, since thermal adjustment rates are on the same order as the Coriolis frequency, Rossby numbers scale both momentum and heat balances, and separate vertical mixing and pressure effects. Detailed comparisons of theory and observations will be reported in future contributions, as will be transfer and impulse response functions in different regions and hemisphere, and their dependences on season and background atmospheric states. Important issues to be addressed in the theory are (i) the roles of geostrophic spindown (Kilpatrick et al. 2016), (ii) ocean currents and (iii) equilibrium responses of vertical mixing. For zero Rossby number the observed wind curl does not vanish, as expected from spindown (Schneider and Qiu 2015). In the Southern Ocean, background winds change on synoptic time scales of a few days, too fast for complete geostrophic spindown (Feliks et al. 2007, 2011). Second, ocean currents directly affect the wind stress curl and accelerate winds in the direction of ocean currents (Cornillon and Park 2001; Renault et al. 2016,

2017; Takatama and Schneider 2017). Scatterometers measure equivalent neutral winds relative to ocean currents (Cornillon and Park 2001), and combine winds induced by ocean currents and by sea surface temperatures (Renault et al. 2019). Separation of these effects will be challenging, and may require experiments with high-resolution atmospheric and coupled models. Third, the vertical mixing effect in formulation in Eq. (2) ceases outside of the nonequilibrium wake with nonvanishing air-sea temperature differences. Consideration of equilibrium responses to sea surface temperatures of the vertical mixing profile and boundary layer depths due to the convective adjustment (Samelson et al. 2006; Vannière et al. 2017a) introduces additional parameters that characterize the lapse rate beyond the top of the boundary layer and may further illuminate observed wind responses.

The present analysis characterizes wind responses to ocean-mesoscale sea surface temperatures in terms of background winds, length scale and Rossby number. Consideration of other processes may further sharpen the observational results. In particular, variations of the thermal boundary layer depth  $H$  scale the thermal adjustment time  $\gamma^{-1}$  and the relative magnitudes of the pressure and vertical mixing effects [see Eq. (2)], and inform the nondimensional Froude number, thermal adjustment rate, Ekman number and surface drag (Table B1). Simulations of the storm track show a systematic dependence of boundary layer depth on wind direction relative to sea surface temperature fronts (Foussard et al. 2019). Cold winds crossing a front toward warm waters are associated with deep boundary layers and prominent wind divergence due to the pressure effects. In contrast, warm winds blowing toward cold waters lead to shallow boundary layers. The former conditions occur in the cold sector of extratropical cyclones and anchor precipitation on the warm side of the Gulf Stream (Vannière et al. 2017a,b), and call for separate estimations of transfer functions in sectors of extratropical systems.

The separation of the processes in wavenumber space may provide a way forward to resolve dynamics governing the wind divergence in the Gulf Stream region. Three processes are cited: the pressure effect based on the collocation on the warm side of the Gulf Stream of surface wind divergence, precipitation and Laplacian of sea surface temperature (Minobe et al. 2008; Plougonven et al. 2018), the vertical mixing effect based on the collocation of wind divergence and the downwind sea surface temperature gradient (e.g., O'Neill et al. 2017), and atmospheric fronts associated with cyclones (O'Neill et al. 2017, 2018) including their anchoring to the Gulf Stream (Parfitt et al. 2016). Consistent with findings here, these investigations cannot be conducted using longer

time averages but require consideration of synoptic atmospheric variability (O'Neill et al. 2017; Plougonven et al. 2018; O'Neill et al. 2018). The scale and Rossby number dependencies revealed in this study explain wind divergences associated with downstream sea surface temperature gradients are to the lee of Gulf Stream sea surface temperature fronts (O'Neill et al. 2017), while wind divergences associated with Laplacian of air temperatures act on larger scales (Vannière et al. 2017a) and are shifted, in the cold sector of cyclones, downwind of the Gulf Stream (Vannière et al. 2017a,b).

Overall, this study shows that processes governing surface wind responses to ocean-mesoscale sea surface temperature separate in lee and port wavenumber space of transfer functions, but intermingle in physical space, as exemplified by the impulse response functions. The dominance of the vertical mixing and pressure effect depends on the circumstances as described by the Rossby number, distribution of sea surface temperature and background winds. In the midlatitude storm track regions, the latter change rapidly from day to day, so that time averaging smooths the responses of transfer and impulse response functions, and degrades the response patterns so that only collocations of wind speeds and sea surface temperature, and of wind divergence and curl with down- and crosswind components of gradients of sea surface temperature remain. The smoothing effect of time averaging critically depends on the distribution of background winds, particularly its direction, and is expected to be much reduced in the trade wind regions with steady wind directions.

The representation of the surface wind response to ocean-mesoscale sea surface temperatures by transfer or impulse response functions offers new evaluation metrics for the boundary layer formulations and their interactions with the free troposphere and ocean. Analyses of atmospheric and coupled model simulations and of existing and new satellite observations offer exciting opportunities to further understanding of the interaction of ocean-mesoscale variations and the atmosphere.

*Acknowledgments.* Numerous discussions with Bruce Cornuelle, Bo Qiu, Thomas Kilpatrick, Ryusuke Masunaga, and Shang-Ping Xie are gratefully acknowledged, as are comments by Eric Firing, Ryo Furue, Kazuyoshi Kikuchi, Masami Nonaka, Jim Potemra, and Bunmei Taguchi. Constructive reviews by Larry O'Neill and Justin Small greatly improved the manuscript. QuikSCAT and AMSR-E data are prepared by Remote Sensing Systems and sponsored by the NASA Ocean Vector Winds Science Team and by AMSR-E Science Team and the NASA Earth Science MEaSUREs Program. Data are available at [www.remss.com](http://www.remss.com). This research was supported

by National Aeronautics and Space Administration, Grants NNX14AL83G and 80NSSC19K0058, and by the JAMSTEC IPRC Joint Investigations (JJI) and Collaborative Research (JICore). This is SOEST Contribution Number 10993 and IPRC Contribution Number 1448.

## APPENDIX A

### Wind Stress Linearization

The surface wind stress  $\tau_T$  is derived from 10-m equivalent neutral winds

$$\tau_T = \rho_{\text{Air}} c_d |U \hat{\mathbf{e}}_U + \mathbf{u}| (U \hat{\mathbf{e}}_U + \mathbf{u}), \quad (\text{A1})$$

with  $c_d$  the neutral stability drag coefficient (O'Neill et al. 2005). A Taylor expansion of (A1) about  $U \hat{\mathbf{e}}_U$  yields to first (linear) order, stress perturbations  $\tau$

$$[\hat{\mathbf{e}}_U \cdot \tau, (\hat{\mathbf{e}}_3 \times \hat{\mathbf{e}}_U) \cdot \tau] = \rho_{\text{Air}} c_d U [2\hat{\mathbf{e}}_U \cdot \mathbf{u}, (\hat{\mathbf{e}}_3 \times \hat{\mathbf{e}}_U) \cdot \mathbf{u}]. \quad (\text{A2})$$

Per Eq. (A2), transfer functions of lee and port components of linearized stress are proportional to those of lee and port equivalent neutral winds, with an explicit dependence on background wind speed  $U$ , and a factor of 2 for the lee component due to the parabolic functionality of wind speed in Eq. (A1). This difference of proportional factors implies that wind stress divergence, curl, Ekman pumping of Eq. (23), and their transfer functions are not proportional to wind divergence and curl, unless dominated by the lee (or port) wind component only.

## APPENDIX B

### Linear Theory

The linear theory of Schneider and Qiu (2015) couples the heat budget (1) via the pressure and vertical mixing forcing  $\mathbf{F}$  of Eq. (2) to the momentum balance

$$(U \hat{\mathbf{e}}_U) \cdot \nabla \mathbf{u} + \frac{w^*}{H} \partial_s (U \hat{\mathbf{e}}_U) + f \hat{\mathbf{e}}_3 \times \mathbf{u} - \frac{1}{H^2} \partial_s A_m \partial_s \mathbf{u} + g' \nabla h = \mathbf{F} \quad (\text{B1})$$

and continuity equation

$$(U \hat{\mathbf{e}}_U) \cdot \nabla h + H \nabla \cdot \mathbf{u} + \partial_s w^* = 0 \quad (\text{B2})$$

in a layer bounded at the sea surface and inversion by the material surfaces where updrafts  $w^*$  vanish. Equation (B1) includes horizontal advection by the background winds and vertical displacements of background

winds by sea surface temperature-induced updrafts  $w^*$  in sigma coordinates, the Coriolis acceleration, mixing by the background eddy viscosity  $A_m$ , and the acceleration due to sea surface temperature-induced horizontal gradients of inversion height  $\nabla h$  with reduced gravity  $g' = (\Delta\Theta/\Theta_0)g$ , inversion strength  $\Delta\Theta$  and reference absolute temperature  $\Theta_0$ . The horizontal stress at the inversion vanishes, and, at the sea surface, is given by a linear drag law

$$\frac{1}{H} A_m \partial_s \mathbf{u} = \alpha \mathbf{u} \quad \text{at } s = 0 \quad (\text{B3})$$

for background solution and for sea surface temperature-induced winds. In general, the surface drag  $\alpha$  depends on the background wind speed and the stability of the surface layer. Modulations of the latter by ocean-mesoscale sea surface temperatures (Liu et al. 2007; Liu and Xie 2008) have only minor impacts on surface winds (O'Neill et al. 2005, 2010b), and  $\alpha$  is set to a constant.

The background eddy coefficient  $A_m$  is constant in the vertical. Its sensitivity  $A'_m/A_m$  to the air-sea temperature difference increases linearly from 0 at the sea surface and inversion to a maximum positive value at the midpoint of the layer as an approximation to more realistic parabolic profiles of the eddy coefficients (Kilpatrick et al. 2014; Ayet and Redelsperger 2019). A positive vertical slope of  $A'_m$  at the surface is essential for realistic simulations of surface winds. The first term on the right-hand side of an expansion of vertical mixing effect

$$\partial_s [A'_m \partial_s (U \hat{\mathbf{e}}_U)] = (\partial_s A'_m) \partial_s (U \hat{\mathbf{e}}_U) + A'_m \partial_s \partial_s (U \hat{\mathbf{e}}_U) \quad (\text{B4})$$

yields at the surface the observed acceleration lee winds in response to warm ocean-mesoscale sea surface temperatures in Eq. (2). The acceleration due to the second term opposes background winds, and decelerates surface winds.

Background winds are horizontally uniform, and estimated from Ekman dynamics driven by a prescribed geostrophic wind, no flux at the inversion, and drag law (B3) at the sea surface.

The solution is obtained for the Southern Hemisphere, and is governed by five parameters: the Froude number  $U/\sqrt{g'H}$ , the thermal adjustment rate normalized by the Coriolis frequency  $\gamma/|f|$ , the Ekman number  $A_m/|f|H^2$  as the square of the ratio of Ekman depth to layer depth  $H$ , the nondimensional drag  $\alpha/|f|H$ , and the stability dependence of the eddy coefficient relative to the background mixing and inversion strength  $\max[(\Delta\Theta/A_m)A'_m]$ . For the parameters used (Table B1), the background wind speed is  $11 \text{ m s}^{-1}$ , the thermal adjustment time  $\gamma^{-1}$  is 4.5 h, the Ekman depth is 600 m and half of the boundary layer depth of 1182 m, and the dimensional linear drag is

TABLE B1. Nondimensional parameters used to obtain and convert to dimensional form the solution (Fig. 9) of the Schneider and Qiu (2015) theory.

$\frac{U}{c}$	0.55	Froude number
$\frac{A_m}{\sqrt{ f H^2}}$	0.25	Ekman number
$\frac{\gamma}{\sqrt{ f }}$	0.6	Thermal adjustment rate
$\frac{\alpha}{\sqrt{ f H}}$	0.1	Surface drag
$\max\left(\frac{\Delta\Theta}{A_m}, A'_m\right)$	10	Sensitivity of vertical mixing coefficients to air-sea temperature difference
$\sqrt{\frac{\Delta\Theta}{\Theta_0}gH}$	20 m s <sup>-1</sup>	Gravity wave speed <i>c</i>
$\Delta\Theta, \Theta_0$	10, 290 K	Inversion strength, reference absolute temperature
<i>H</i>	1182 m	Boundary layer height, estimated from gravity wave speed and inversion strength
<i>f</i>	−10 <sup>−4</sup> s <sup>−1</sup>	Coriolis frequency at a latitude of 45°S

10<sup>−2</sup> ms<sup>−1</sup> and corresponds to canonical values of 10<sup>−3</sup> for a drag coefficient and 10 ms<sup>−1</sup> wind speed, and a doubling of the vertical eddy coefficient at middepth for a 1-K air-sea temperature difference.

Resulting background winds form a modified Ekman spiral (Holton 2004), scaled to 11 ms<sup>−1</sup> surface and 12.2 ms<sup>−1</sup> geostrophic winds, with the latter 6.7° to the left of the former (heavy arrow in Fig. 9a). Between surface and inversion, the Ekman spiral has a shear in wind speed of 1.75 ms<sup>−1</sup> and anticyclonic change in direction of 3° (Fig. 9b). The vertical vector-averaged winds blow 1.4° left of surface winds at 12.1 ms<sup>−1</sup> (Fig. 9c).

REFERENCES

Ayet, A., and J.-L. Redelsperger, 2019: An analytical study of the atmospheric boundary-layer flow and divergence over an SST front. *Quart. J. Roy. Meteor. Soc.*, **145**, 2549–2567, <https://doi.org/10.1002/qj.3578>.

Bryan, F. O., R. Tomas, J. M. Dennis, D. B. Chelton, N. G. Loeb, and J. L. McClean, 2010: Frontal scale air-sea interaction in high-resolution coupled climate models. *J. Climate*, **23**, 6277–6291, <https://doi.org/10.1175/2010JCLI3665.1>.

Chelton, D. B., and S. P. Xie, 2010: Coupled ocean-atmosphere interaction at oceanic mesoscales. *Oceanography*, **23** (4), 52–69, <https://doi.org/10.5670/oceanog.2010.05>.

—, and Coauthors, 2001: Observations of coupling between surface wind stress and sea surface temperature in the eastern tropical Pacific. *J. Climate*, **14**, 1479–1498, [https://doi.org/10.1175/1520-0442\(2001\)014<1479:OOCBSW>2.0.CO;2](https://doi.org/10.1175/1520-0442(2001)014<1479:OOCBSW>2.0.CO;2).

—, M. G. Schlax, M. H. Freilich, and R. F. Milliff, 2004: Satellite measurements reveal persistent small-scale features in ocean winds. *Science*, **303**, 978–983, <https://doi.org/10.1126/science.1091901>.

Cornillon, P., and K. Park, 2001: Warm core ring velocities inferred from NSCAT. *Geophys. Res. Lett.*, **28**, 575–578, <https://doi.org/10.1029/2000GL011487>.

Fairall, C., E. F. Bradley, J. Hare, A. Grachev, and J. Edson, 2003: Bulk parameterization of air-sea fluxes: Updates and verification for the COARE algorithm. *J. Climate*, **16**, 571–591, [https://doi.org/10.1175/1520-0442\(2003\)016<0571:BPOASF>2.0.CO;2](https://doi.org/10.1175/1520-0442(2003)016<0571:BPOASF>2.0.CO;2).

Feliks, Y., M. Ghil, and E. Simonnet, 2004: Low-frequency variability in the midlatitude atmosphere induced by an oceanic thermal front. *J. Atmos. Sci.*, **61**, 961–981, [https://doi.org/10.1175/1520-0469\(2004\)061<0961:LVTMA>2.0.CO;2](https://doi.org/10.1175/1520-0469(2004)061<0961:LVTMA>2.0.CO;2).

—, —, and —, 2007: Low-frequency variability in the midlatitude baroclinic atmosphere induced by an oceanic thermal front. *J. Atmos. Sci.*, **64**, 97–116, <https://doi.org/10.1175/JAS3780.1>.

—, —, and A. Robertson, 2011: The atmospheric circulation over the North Atlantic as induced by the SST field. *J. Climate*, **24**, 522–542, <https://doi.org/10.1175/2010JCLI3859.1>.

Foussard, A., G. Lapeyre, and R. Plougonven, 2019: Response of surface wind divergence to mesoscale SST anomalies under different wind conditions. *J. Atmos. Sci.*, **76**, 2065–2082, <https://doi.org/10.1175/JAS-D-18-0204.1>.

Frenger, I., N. Gruber, R. Knutti, and M. Munnich, 2013: Imprint of Southern Ocean eddies on winds, clouds and rainfall. *Nat. Geosci.*, **6**, 608–612, <https://doi.org/10.1038/ngeo1863>.

Gaube, P., D. B. Chelton, R. M. Samelson, M. G. Schlax, and L. W. O. Neill, 2015: Satellite observations of mesoscale eddy-induced Ekman pumping. *J. Phys. Oceanogr.*, **45**, 104–132, <https://doi.org/10.1175/JPO-D-14-0032.1>.

Hausmann, U., and A. Czaja, 2012: The observed signature of mesoscale eddies in sea surface temperature and the associated heat transport. *Deep-Sea Res. I*, **70**, 60–72, <https://doi.org/10.1016/j.dsr.2012.08.005>.

Hayes, S., M. McPhaden, and J. Wallace, 1989: The influence of sea-surface temperature on surface wind in the eastern equatorial Pacific: Weekly to monthly variability. *J. Climate*, **2**, 1500–1506, [https://doi.org/10.1175/1520-0442\(1989\)002<1500:TIOSSST>2.0.CO;2](https://doi.org/10.1175/1520-0442(1989)002<1500:TIOSSST>2.0.CO;2).

Holton, J. R., 2004: *An Introduction to Dynamic Meteorology*. Academic Press, 535 pp.

Kilpatrick, T., N. Schneider, and B. Qiu, 2014: Boundary layer convergence induced by strong winds across a midlatitude SST front. *J. Climate*, **27**, 1698–1718, <https://doi.org/10.1175/JCLI-D-13-00101.1>.

—, —, and —, 2016: Atmospheric response to a midlatitude SST front: Alongfront winds. *J. Atmos. Sci.*, **73**, 3489–3509, <https://doi.org/10.1175/JAS-D-15-0312.1>.

Lambaerts, J., G. Lapeyre, R. Plougonven, and P. Klein, 2013: Atmospheric response to sea surface temperature mesoscale structures. *J. Geophys. Res. Atmos.*, **118**, 9611–9621, <https://doi.org/10.1002/jgrd.50769>.

Laurindo, L. C., L. Siqueira, A. J. Mariano, and B. P. Kirtman, 2019: Cross-spectral analysis of the SST/10-m wind speed coupling resolved by satellite products and climate model simulations. *Climate Dyn.*, **52**, 5071–5098, <https://doi.org/10.1007/s00382-018-4434-6>.

Lindzen, R. S., and S. Nigam, 1987: On the role of sea-surface temperature-gradients in forcing low-level winds and convergence in the tropics. *J. Atmos. Sci.*, **44**, 2418–2436, [https://doi.org/10.1175/1520-0469\(1987\)044<2418:OTROSS>2.0.CO;2](https://doi.org/10.1175/1520-0469(1987)044<2418:OTROSS>2.0.CO;2).

Liu, W. T., and W. Tang, 1996: Equivalent neutral wind. Jet Propulsion Laboratory Publ. 96-17, 22 pp.

—, and X. Xie, 2008: Ocean-atmosphere momentum coupling in the Kuroshio extension observed from space. *J. Oceanogr.*, **64**, 631–637, <https://doi.org/10.1007/s10872-008-0053-x>.

—, —, and P. P. Niiler, 2007: Ocean-atmosphere interaction over Agulhas extension meanders. *J. Climate*, **20**, 5784–5797, <https://doi.org/10.1175/2007JCLI1732.1>.

- Maloney, E. D., and D. B. Chelton, 2006: An assessment of the sea surface temperature influence on surface wind stress in numerical weather prediction and climate models. *J. Climate*, **19**, 2743–2762, <https://doi.org/10.1175/JCLI3728.1>.
- Minobe, S., A. Kuwano-Yoshida, N. Komori, S.-P. Xie, and R. J. Small, 2008: Influence of the Gulf Stream on the troposphere. *Nature*, **452**, 206–209, <https://doi.org/10.1038/nature06690>.
- O'Neill, L. W., 2012: Wind speed and stability effects on coupling between surface wind stress and SST observed from buoys and satellite. *J. Climate*, **25**, 1544–1569, <https://doi.org/10.1175/JCLI-D-11-00121.1>.
- , D. B. Chelton, and S. K. Esbensen, 2003: Observations of SST-induced perturbations of the wind stress field over the Southern Ocean on seasonal timescales. *J. Climate*, **16**, 2340–2354, <https://doi.org/10.1175/2780.1>.
- , —, —, and F. J. Wentz, 2005: High-resolution satellite measurements of the atmospheric boundary layer response to SST variations along the Agulhas Return Current. *J. Climate*, **18**, 2706–2723, <https://doi.org/10.1175/JCLI3415.1>.
- , —, and —, 2010a: The effects of SST-induced surface wind speed and direction gradients on midlatitude surface vorticity and divergence. *J. Climate*, **23**, 255–281, <https://doi.org/10.1175/2009JCLI2613.1>.
- , S. K. Esbensen, N. Thum, R. M. Samelson, and D. B. Chelton, 2010b: Dynamical analysis of the boundary layer and surface wind responses to mesoscale SST perturbations. *J. Climate*, **23**, 559–581, <https://doi.org/10.1175/2009JCLI2662.1>.
- , D. B. Chelton, and S. K. Esbensen, 2012: Covariability of surface wind and stress responses to sea surface temperature fronts. *J. Climate*, **25**, 5916–5942, <https://doi.org/10.1175/JCLI-D-11-00230.1>.
- , T. Haack, D. B. Chelton, and E. Skillingstad, 2017: The Gulf Stream convergence zone in the time-mean winds. *J. Atmos. Sci.*, **74**, 2383–2412, <https://doi.org/10.1175/JAS-D-16-0213.1>.
- , —, —, and —, 2018: Reply to “Comments on ‘The Gulf Stream convergence zone in the time-mean winds.’” *J. Atmos. Sci.*, **75**, 2151–2153, <https://doi.org/10.1175/JAS-D-18-0044.1>.
- Parfitt, R., A. Czaja, S. Minobe, and A. Kuwano-Yoshida, 2016: The atmospheric frontal response to SST perturbations in the Gulf Stream region. *Geophys. Res. Lett.*, **43**, 2299–2306, <https://doi.org/10.1002/2016GL067723>.
- Plougonven, R., A. Foussard, and G. Lapeyre, 2018: Comments on “The Gulf Stream convergence zone in the time-mean winds.” *J. Atmos. Sci.*, **75**, 2139–2149, <https://doi.org/10.1175/JAS-D-17-0369.1>.
- Renault, L., M. J. Molemaker, J. C. McWilliams, A. F. Shchepetkin, F. Lemarié, D. Chelton, S. Illig, and A. Hall, 2016: Modulation of wind work by oceanic current interaction with the atmosphere. *J. Phys. Oceanogr.*, **46**, 1685–1704, <https://doi.org/10.1175/JPO-D-15-0232.1>.
- , J. C. McWilliams, and S. Masson, 2017: Satellite observations of imprint of oceanic current on wind stress by air-sea coupling. *Sci. Rep.*, **7**, 17747, <https://doi.org/10.1038/s41598-017-17939-1>.
- , S. Masson, V. Oerder, S. Jullien, and F. Colas, 2019: Disentangling the mesoscale ocean-atmosphere interactions. *J. Geophys. Res. Oceans*, **124**, 2164–2178, <https://doi.org/10.1029/2018JC014628>.
- Ricciardulli, L., F. J. Wentz, and D. K. Smith, 2011: Remote sensing systems QuikSCAT Ku-2011 daily, ocean vector winds on 0.25 deg grid, version 4. Remote Sensing Systems, accessed 6 November 2014, [www.remss.com/missions/quikscat](http://www.remss.com/missions/quikscat).
- Samelson, R. M., E. D. Skillingstad, D. B. Chelton, S. K. Esbensen, L. W. O'Neill, and N. Thum, 2006: On the coupling of wind stress and sea surface temperature. *J. Climate*, **19**, 1557–1566, <https://doi.org/10.1175/JCLI3682.1>.
- Schneider, N., and B. Qiu, 2015: The atmospheric response to weak sea surface temperature fronts. *J. Atmos. Sci.*, **72**, 3356–3377, <https://doi.org/10.1175/JAS-D-14-0212.1>.
- Schubert, W. H., J. S. Wakefield, E. J. Steiner, and S. K. Cox, 1979: Marine stratocumulus convection. Part II: Horizontally inhomogeneous solutions. *J. Atmos. Sci.*, **36**, 1308–1324, [https://doi.org/10.1175/1520-0469\(1979\)036<1308:MSPH>2.0.CO;2](https://doi.org/10.1175/1520-0469(1979)036<1308:MSPH>2.0.CO;2).
- Seo, H., A. J. Miller, and J. O. Roads, 2007: The Scripps Coupled Ocean–Atmosphere Regional (SCOAR) model, with applications in the eastern Pacific sector. *J. Climate*, **20**, 381–402, <https://doi.org/10.1175/JCLI4016.1>.
- Small, R. J., S.-P. Xie, and Y. Wang, 2003: Numerical simulation of atmospheric response to Pacific tropical instability waves. *J. Climate*, **16**, 3723–3741, [https://doi.org/10.1175/1520-0442\(2003\)016<3723:NSOART>2.0.CO;2](https://doi.org/10.1175/1520-0442(2003)016<3723:NSOART>2.0.CO;2).
- , —, and J. Hafner, 2005: Satellite observations of mesoscale ocean features and copropagating atmospheric surface fields in the tropical belt. *J. Geophys. Res.*, **110**, C02021, <https://doi.org/10.1029/2004JC002598>.
- , and Coauthors, 2008: Air-sea interaction over ocean fronts and eddies. *Dyn. Atmos. Oceans*, **45**, 274–319, <https://doi.org/10.1016/j.dynatmoce.2008.01.001>.
- Song, Q., D. B. Chelton, S. K. Esbensen, N. Thum, and L. W. O'Neill, 2009: Coupling between sea surface temperature and low-level winds in mesoscale numerical models. *J. Climate*, **22**, 146–164, <https://doi.org/10.1175/2008JCLI2488.1>.
- Spall, M. A., 2007: Midlatitude wind stress–sea surface temperature coupling in the vicinity of oceanic fronts. *J. Climate*, **20**, 3785–3801, <https://doi.org/10.1175/JCLI4234.1>.
- Takatama, K., and N. Schneider, 2017: The role of back pressure in the atmospheric response to surface stress induced by the Kuroshio. *J. Atmos. Sci.*, **74**, 597–615, <https://doi.org/10.1175/JAS-D-16-0149.1>.
- Vanni re, B., A. Czaja, H. Dacre, and T. Woollings, 2017a: A cold path for the Gulf Stream–troposphere connection. *J. Climate*, **30**, 1363–1379, <https://doi.org/10.1175/JCLI-D-15-0749.1>.
- , —, and —, 2017b: Contribution of the cold sector of extratropical cyclones to mean state features over the Gulf Stream in winter. *Quart. J. Roy. Meteor. Soc.*, **143**, 1990–2000, <https://doi.org/10.1002/qj.3058>.
- Wallace, J. M., T. P. Mitchell, and C. Deser, 1989: The influence of sea-surface temperature on surface wind in the eastern equatorial Pacific: Seasonal and interannual variability. *J. Climate*, **2**, 1492–1499, [https://doi.org/10.1175/1520-0442\(1989\)002<1492:TIOSST>2.0.CO;2](https://doi.org/10.1175/1520-0442(1989)002<1492:TIOSST>2.0.CO;2).
- Wenegrat, J., and R. Arthur, 2018: Response of the atmospheric boundary layer to submesoscale sea surface temperature fronts. *Geophys. Res. Lett.*, **45**, 13–505, <https://doi.org/10.1029/2018GL081034>.
- Wentz, F. J., T. Meissner, C. Gentemann, and M. Brewer, 2014: Remote sensing systems AQUA AMSR-E 3-day environmental suite on 0.25 deg grid, version V.7. Remote Sensing Systems, accessed 1 May 2014, [www.remss.com/missions/amr](http://www.remss.com/missions/amr).
- , and Coauthors, 2017: Evaluating and extending the ocean wind climate data record. *IEEE J. Sel. Top. Appl. Earth Obs. Remote Sens.*, **10**, 2165–2185, <https://doi.org/10.1109/JSTARS.2016.2643641>.
- Wunsch, C., 1996: *The Ocean Circulation Inverse Problem*. Cambridge University Press, 442 pp.
- Xie, S.-P., 2004: Satellite observations of cool ocean–atmosphere interaction. *Bull. Amer. Meteor. Soc.*, **85**, 195–208, <https://doi.org/10.1175/BAMS-85-2-195>.